Seasonally-Managed Wetland Footprint Delineation using Landsat ETM+ Satellite Imagery

Nigel W.T. Quinn PhD, P.E., D.WRE
Lawrence Berkeley National Laboratory
1 Cyclotron Road, Bld.14-134
Berkeley, CA 94720, USA

and

Olga Epshtein
School of Sustainable Engineering and the Built Environment
Arizona State University,
Tempe, AZ 85287, USA

January 12, 2014

This work was supported by the U.S. Bureau of Reclamation under US Department of Interior Interagency Agreement No. 3-AA-20-10970, through Contract No. DE-AC02-05CH11231 between Lawrence Berkeley National Laboratory and the U. S. Department of Energy.

ACKNOWLEDGEMENTS

This work was supported by the U.S. Department of Energy, Center for Science and Engineering Education and the U.S. Bureau of Reclamation, Science and Technology Program and MP-400. Our gratitude is extended to Chuck Johnson for his continued support of our wetland ET research program and to Linda Colella, MP-400 for maintaining the wetland sensor research program initiated by the late Mike Heaton. Thanks to Ric Ortega, General Manager, Grassland Water District for his technical support and provision of south Grassland Water District wetland monitoring data. Thanks also to Professor Luis Garcia, Director of the Integrated Decision Support Group at Colorado State University and Dr. Aymn Elhaddad for provision of the ReSET model and for user support. We also wish to acknowledge Dr. Richard Snyder and Professor Susan Ustin (Department of Land, Air and Water Resources, University of California, Davis), for valuable input.

DISCLAIMER

This document was prepared as an account of work sponsored by the United States Government. While this document is believed to contain correct information, neither the United States Government nor any agency thereof, nor the Regents of the University of California, nor any of their employees, makes any warranty, express or implied, or assumes any legal responsibility for the accuracy, completeness, or usefulness of any information, apparatus, product, or process disclosed, or represents that its use would not infringe privately owned rights. Reference herein to any specific commercial product, process, or service by its trade name, trademark, manufacturer, or otherwise, does not necessarily constitute or imply its endorsement, recommendation, or favoring by the United States Government or any agency thereof, or the Regents of the University of California. The views and opinions of authors expressed herein do not necessarily state or reflect those of the United States Government or any agency thereof or the Regents of the University of California.

Seasonally-Managed Wetland Footprint Delineation in the western San Joaquin Basin, California using Landsat ETM+ Satellite Imagery

Nigel W.T. Quinn PhD, P.E., D.WRE
Lawrence Berkeley National Laboratory
1 Cyclotron Road, Bld.14-134
Berkeley, CA 94720, USA

Olga Epshtein
[b]School of Sustainable Engineering and the Built Environment
Arizona State University,
Tempe, AZ 85287, USA

Published in the Elsevier Journal of Environmental Modelling and Software.
Vol. 54, April 2014, pp 9-23.
http://dx.doi.org/10.1016/j.envsoft.2013.12.012

Corresponding author Quinn at: Lawrence Berkeley National Laboratory, 1 Cyclotron Road, Bld.14-132, Berkeley, CA 94720, USA. Tel.: +1 510 486 7056; fax: + 1 510 486 7152. Email address: nwquinn@lbl.gov (N.W.T. Quinn).

Abstract

One major challenge in water resource management is the estimation of evapotranspiration losses from seasonally managed wetlands. Quantifying these losses is complicated by the dynamic nature of the wetlands' areal footprint during the periods of flood-up and drawdown. In this study we present a data-lean solution to this problem using an example application in the San Joaquin River Basin of California, USA. Through analysis of high-resolution (30 meter) Landsat Enhanced Thematic Mapper Plus (ETM+) satellite imagery, we develop a metric for more fully capturing the extent of total flooded wetland area. The procedure is validated using year-long, continuously-logged field datasets at two separate wetlands within the study area. Based on this record, the proposed classification using a Landsat ETM+ Band 5 (mid-IR wavelength) to Band 2 (visible green wavelength) ratio improves estimates by 30-50% relative to previous attempts at wetland delineation. Requiring modest ancillary data, the results of our study provide a practical and efficient option for wetland management in data-sparse regions or un-gauged watersheds.

Keywords:

Remote Sensing, Environmental Decision Support, Water Resource Management, Wetlands, Ecohydrology, Basin Hydrology

Highlights

- A method to delineate seasonal wetlands in the San Joaquin Basin is proposed.
- Surface temperature differs between open water, flooded and terrestrial vegetation.
- A Landsat ETM+ 5/2 band ratio improves wetland delineation up to 50%.
- Classification is corroborated using year-long field-based datasets.

1. Introduction

Seasonally managed wetlands are man-made impoundments that undergo a complex hydrologic cycle of inundation and drainage designed to mimic natural ecohydrologic function. In seasonally managed wetlands, changes associated with standing water inundation and vegetation response also play a role in energy cycling, by influencing solar radiation partitioning into latent heat by plant transpiration and thermal energy storage in the water column. Prevailing climate and temperature conditions determine the timing of the annual progression of wetland flooding, holding, and draw down. The areal extent of the wetland during this cycle is known as the "wetland footprint." At any point in time, direct evaporation, transpiration, and seepage (soil infiltration) losses from the wetlands are a function of their footprint.

During flood-up, the footprint gradually expands as water is diverted into each impoundment until the pond is filled to an elevation set by weir boards at the pond outlet. As the pond begins to fill, the clay-rich soils which had become desiccated during the dewatering period provide a dense network of preferential flow paths. This results in significant losses to soil infiltration. As wetland sediments become fully saturated, the clay soils swell and "seal". In response to increased soil water availability, plant community composition shifts; macrophytes begin to displace terrestrial grasses; emergent wetland vegetation grows to pond shooting depth, and transpiration increases. Similarly, during wetland drawdown, pond sediments become exposed to the atmosphere as water elevation recedes until there is no further outflow from the pond. Infiltration, direct water and soil evaporation, and plant transpiration rates undergo another shift.

The temporal and spatial dynamics of these losses are resource-intensive to measure in the field and difficult to accurately quantify through indirect methods. Yet despite the challenge, these dynamics are crucial for informed, science-based wetland management – both from a water resource allocation and an ecosystem function perspective. This paper examines the potential for satellite imagery and image processing thermal algorithms to provide a signal consistently differentiating open water, bare soil, emergent wetland vegetation, and terrestrial vegetation. A successful methodology would result in improved estimates of the dynamic "wetland footprint."

1.1. *Applications of Remote Sensing to Wetland and Land-Water Interface Delineation*

Remote sensing offers the potential to track temporal changes in wetland hydrology, chemistry, and vegetation dynamics, thereby accounting for fluxes in water and constituent cycling. Multispectral imagery has been successfully used in the past for year-round open water delineation, as well as for vegetation classification and change detection in a variety of ecosystems. Mapping studies by Lunetta and Balogh (1999), Berberoglu *et al.* (2004), Klemas (2005), Phillips *et al.* (2005), Frohn *et al.* (2009), and Klemas (2011), have demonstrated the potential of applying remote sensing methods to wetland identification. None of these, however, were concerned with the wetland footprint as a direct foundation for water management decision-making based on modeled simulations of water quality. Whereas delineation of open water and general vegetation characterization is sufficient for wetland identification, the objectives of our study required capturing the wetland footprint transparently and consistently enough to aid in decision-support.

The feedbacks between vegetation characteristics and environmental function of wetland ecosystems were studied by Kokaly *et al*. (2003) and Lin and Liquan (2006). These studies illustrate how vegetation characteristics such as density, vitality, and spatial extent may serve as important ecohydrologic indicators. Remote sensing-based vegetation mapping by Macleod and Congalton (1998), Phinn *et al.* (1999), Harvey and Hill (2001), and Schmidt *et al.* (2004) has been successful at a number of spatial scales. While we can base the legitimacy of remote sensing-based approaches for wetland analysis on these and more recent studies, they have been particularly effective in permanent wetlands in which vegetation composition and extent of flooded area remain relatively static throughout the year. Though permanent wetlands are subject to water losses to infiltration, evaporation, and plant transpiration, they are rarely – if ever - completely dewatered. Conversely, in seasonal wetlands inundation and dewatering occur with regularity and represent a key boundary condition regulating both the ecologic and hydrologic response of the system. This hydrologic seasonality exerts an important control on plant community composition, transpiration, and spectral characteristics. However, time-lags between the recession of water and the vegetation community's response create additional complexity.

We aimed to address these important limitations by developing methods appropriate to seasonal wetlands.

Though coastal and wetland systems are not identical, there is some overlap, particularly in the delineation of the land-water interface. Klemas (2013) provides an overview of the latest airborne remote sensing methods applied to the analysis of coastal features and processes. Many techniques, such as close-range aerial photography, airborne LiDAR surveys, kinematic differential GPS post-processing, and airborne hyperspectral imagery, are compatible with wetland delineation. However, the accuracy of many land-water interface delineation methods in wetland systems is limited by the spatial resolution of the satellite imagery, spectral signature overlap between wetland vegetation species, and by the high ecological complexity and spatial irregularity of the wetlands (Ozesmi and Bauer, 2002).

Since Ozesmi and Bauer's review, image processing techniques have improved. The efforts driving these developments can be grouped into two main camps. The first is concerned with computational methods and signal processing. Baker *et al.* (2006) and Wright and Gallant (2007) used classification trees, a computational technique which originated in computational biology but has since spread to other fields as well, to combine Landsat imagery with field-based observations. The authors found that while ancillary environmental data improved classification accuracies, hard classification remained problematic. Wright and Gallant concluded that probability landscapes, rather than hard classification, may be the more practical approach to classifying wetlands. Similarly, pixel classification using artificial neural networks is quite promising for deciphering the spatial and temporal dynamics of wetland ecosystems. However, based on the work of Bagan *et al.* (2005), Ĉerná and Chytrý (2005), and Xie *et al*. (2008), neural network analysis becomes very computationally expensive for all but the smallest datasets.

Approaching the problem from a function, rather than process, perspective, others have sought to inform remote sensing by drawing on methods from landscape ecology. Cushman *et al.* (2008) and Kelly *et al.* (2011) looked at using landscape metrics as proxies for ecologic characterization to aid in wetland delineation. Such approaches are well-suited for analysis over broad spatial scales, yet have an important limitation. The authors conclude that due to the variability of both

structural and functional landscape characteristics, the identification of appropriate matrices for a given study area may well form a separate study in itself. As such, pattern metrics are not readily generalizable across geographic regions.

Alongside advances in image processing, higher resolution imagery has become more readily available both from commercial vendors and through further advances in airborne, rather than satellite, sensors. Maxa and Bolstad (2009) employed high resolution IKONOS satellite imagery merged with 1-meter resolution LiDAR data to map and classify wetlands in the Wisconsin Wetland Inventory. LiDAR data was also used by Cook *et al.* (2009) in conjunction with ultra-fine precision commercial QuickBird imagery to estimate wetland plant productivity. Adam *et al.* (2010) review recent multispectral and hyperspectral remote sensing wetland studies, noting in particular the advantages of remote sensing data acquisition via hand-held sensors. These improvements, driven in part by advances in mechanical and optical engineering, are valuable contributions to the field. Nevertheless, the cost of commercial imagery or airborne sensor deployment remains an obstacle and hinders the application of higher-resolution imagery in studies requiring multi-temporal analysis for monitoring and evaluation of highly dynamic systems. Cost is of particular concern for studies at large spatial scales, such as river basins, and when regulatory pressures and an increasingly constrained water management environment provide the motivation, but not the resources, to execute the analysis.

1.2. Study Area

To better understand the feedbacks between energy and water fluxes as they relate to mapping the dynamic wetland "footprint," and to demonstrate how a better understanding could improve response to environmental regulation, a region of the Sacramento-San Joaquin River Delta of California was chosen as a case study. The Sacramento-San Joaquin Delta covers 840,000 acres of floodplain estuary lying at the confluence of the Sacramento and San Joaquin River basins. Suisun Marsh forms the largest continuous brackish water marsh in the western United States and contains more than 10 percent of California's remaining natural wetlands (DWR, 2008). Both marsh and delta lie along key migration paths of anadromous fish and wildfowl on the Pacific Flyway. Peat soils, abundant water supplies, and a moderate marine climate contribute to high agricultural productivity. In addition to being a vital ecological and agricultural resource,

the Delta serves California's two largest water systems - the federal Central Valley Project and the State Water Project. Its water exports maintain managed wetlands and riparian corridors both within and upstream of the Delta, support two-thirds of the state's urban population, and irrigate 3-million acres of agricultural land state-wide (DWR, 2008).

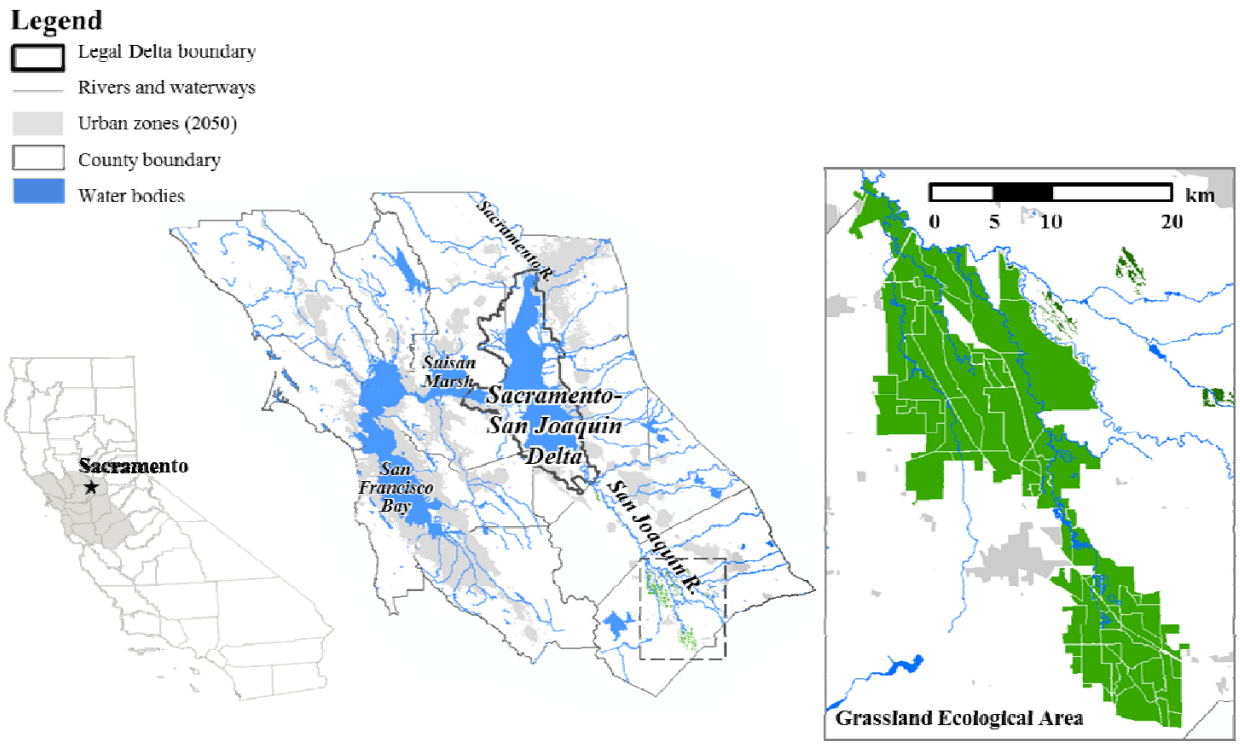

Figure 1: The Sacramento and San Joaquin River Basins drain to the Sacramento-San Joaquin Delta (center image). Within the Delta, the Grassland Ecological Area (right-most image) encompasses over 77,000 hectares of seasonal and permanent wetlands. These wetlands are used as the case study presented in this paper.

Within the San Joaquin River Basin portion of the greater Delta area, the Grasslands Ecological Area (GEA) forms a contiguous mixture of 77,000 hectares of seasonal and permanent wetlands (Figure 1, right-most inset). Once part of a much larger wetland complex, the GEA is now actively managed as wildfowl habitat. Throughout the San Joaquin River Basin, water deliveries from the San Joaquin River and imports from the Delta support wild and aquatic life, managed wetland vegetation, agriculture, grazing, and municipal and industrial uses – resulting in a highly constrained, over-allocated system.

1.3. *Application in Basin-Scale Water Quality Management Decision Support Systems*

Adaptive resource management is a technique of "learning-by-doing" which is increasingly being used to push back at regulatory pressures that reduce operational flexibility. Within the study area, real-time water quality management seeks to improve compliance with San Joaquin River salinity objectives by better coordination of saline drainage from the west-side of the San Joaquin Basin with high quality reservoir releases from the east-side of the Basin (Quinn and Karkoski, 1998; Quinn, 2009; Quinn *et al*., 2010 a-c). Implementation of real-time water quality management will rely on web-sharing of flow and water quality (salinity) monitoring data on public sites such as the California Data Exchange, and commercial remote monitoring and sensor control platforms such as YSI-EcoNET (YSI/Xylem, 2012). Currently, a YSI-EcoNET application in the Grassland Ecological Area provides real-time access to data sampled at a 15-minute resolution from 46 flow and salinity monitoring stations. These data are passed into WISKI (KISTERS North America Inc., 2011) for analysis and validation. Following QA, the data are exported to an FTP site owned by the U.S. Bureau of Reclamation.

Data from this system are being used to calibrate a wetland management model of the Grassland Ecological Area. The model will perform daily water and salinity balances of wetland subareas that receive water supply from the same canals and that drain to the same drainage channels. Wetland inflow and outflow are tracked using the system of distributed field sensors. These data are used to simulate wetland evapotranspiration and seepage as well as daily changes in pond storage. Numerical simulation of water and salinity balances in these wetland subareas is necessary because it would be too costly and time consuming to construct monitoring stations at each pond inlet and outlet. The simulation model will provide decision support to wetland managers with responsibility for meeting salinity load objectives that will eventually be set for the State and Federal wildlife refuges and private wetland entities that make up the Grassland Ecological Area.

The primary goal of this study was to develop an efficient and robust method to capture the dynamics of the wetland footprint. Wetland delineation and remote sensing-based evapotranspiration estimates will (1) support the development of a real-time GEA wetland simulation model, and (2) lay the foundations for a basin-scale water resource management

decision-support model in the San Joaquin Basin. Consequently, the approach was to be both computationally and financially inexpensive, readily applicable, and able to garner support from a wide range of stakeholders; among them, water managers, state and federal environmental regulatory agencies, and agricultural users. Insofar as it is achieves these aims and remains generalizable to other climates and ecologic regimes, the methods presented in this paper are of use to others tasked with the important issue of water resource management in wetland systems (USEPA, 2002). In the following sections, the theoretical framework and data processing methodology is laid out, and the final procedure for delineating the wetland footprint is discussed. This is followed by a performance assessment based on field data from a matched study of two separate wetlands within the GEA. Finally, current limitations pertaining to the applicability of these methods to wetland systems at large are summarized.

2. Methods

2.1. *Theoretical Framework*

The wetland "footprint" was derived using ERDAS Imagine to process a year-long dataset of multispectral Landsat 7 Enhanced Thematic Mapper Plus (ETM +) satellite imagery captured over the course of wetland flood-up and drawdown. Thermal image-processing algorithms were expected to provide a discernible signal to separate water covered by emergent vegetation from terrestrial vegetation and upland areas. Ideally, this approach would allow mapping the total extent of wetland inundation, overcoming the limitations posed by analysis of vegetation spectral signal alone. This study tested whether ground surface temperature can be used as proxy for standing water availability; and if so, whether this approach could be used to track wetland ponds through different stages of inundation.

The change of state of water during the process of wetland open water evaporation and plant transpiration produces a drop in air temperature above the pond surface and above and around the transpiring plant. Consequently, remotely-sensed surface temperature and sensible heat flux of actively transpiring, vegetated pixels were expected to show lower values than those of adjacent, non-vegetated, non-transpiring areas. Terrestrial vegetation, even with a shallow

groundwater table common beneath wetlands, will generally be more water-limited than flooded emergent vegetation. Consequently, vegetation growing outside inundated zones will transpire at lower rates or shut off transpiration more frequently. Decreased evapotranspiration (ET) results in less evaporative cooling and produces correspondingly higher surface temperature. While this is a common assumption for croplands (Burman *et al*., 1986), it also holds true for other types of vegetation (Porporato *et al*., 2001), such as the moist soil plant vegetation associated with seasonal wetlands. Furthermore, open water evaporation rates will generally exceed soil evaporation – particularly in cases where terrestrial vegetation shields soils from direct radiation. Transforming a multispectral Landsat ETM+ image into a spatially-distributed grid of surface temperature values was expected to produce different signals for each of the categories of interest – open water, emergent vegetation, terrestrial vegetation, and bare soil. Applied to a sequence of Landsat images, this classification could be used for mapping flood-up extent and seasonal progression of wetland inundation.

Despite the dominant effect of water availability on ET rates, the cycles of inundation and draw-down combined with the growth rates of wetland vegetation create a highly dynamic system with multiple feedback loops (Drexler *et al*., 2003). The GEA wetlands are complex systems both spatially (network of irregular ponds) and functionally (high inter-pond vegetation diversity and intra-pond community spatial variability). Both factors were expected to influence plant function, water and energy cycling, and expected thermal output (Donohue *et al*., 2007). As a result, the methods used in this study also tested (by proxy) whether GEA wetland habitat is sufficiently functionally homogeneous to validate the conceptual model or whether other factors, such as species composition, may exert a dominant effect on the thermal signal and mask that associated with standing water.

2.2. *ReSET and Thermal Data Processing*

Evapotranspiration was calculated using a series of thermal algorithms in ReSET (Remote Sensing of Evapotranspiration). ReSET is a satellite image-processing program developed by the Integrated Decision Support (IDS) Group at Colorado State University. The program is complimentary to other remote sensing-based evapotranspiration models that have been

developed to provide high-resolution evapotranspiration estimates for large study areas. ReSET is most closely based on METRIC (Mapping Evapotranspiration at High Resolution, developed by Allen *et al*., 2007), which in turn came into being as an offshoot of SEBAL (Surface Energy Balance Algorithm for Land, initially developed by Bastiaanssen *et al*., 1998). Similarly to its predecessors, ReSET uses the thermal infrared Landsat band and vegetation reflectance to calculate a spatially-distributed grid of instantaneous ET loss estimates (Elhaddad and Garcia, 2007, 2008). In basin-scale applications, the daily contributions of ET losses to the water balance from individual wetland ponds are an aggregation of discrete point-scale ET values within a processed satellite image, clipped to exclude open water surface area. Open water evaporation is estimated from monitored pan evaporation rate data and scaled according to the ratio of surface area between the evaporation pan and wetland.

Landsat 7 (ETM +) scenes were collected for the study area to generate a year-long dataset (Table 1). Landsat ETM+ images consist of eight spectral bands with a spatial resolution of 30 meters for bands 1-5 and band 7. Bands 1-3 collect radiation in the visible spectrum, detecting the spectral response of visible blue (band 1), green (band 2), and red (band 3) wavelengths. Bands 4-7 collect data in the near infrared (band 4), middle infrared (bands 5 and 7) and thermal infrared (band 6, 60-meter resolution) wavelengths. Band 8 is a panchromatic (grayscale) band that detects the visible red, green and blue portions of the electromagnetic spectrum. Captured at a resolution of 15 meters, band 8 is used for image sharpening. Thermal infrared (band 6) is collected at two separate gain settings at once; the low gain (band 6(1)) setting was used in ReSET. Although low gain results in a somewhat lower resolution, the band 6(1) signal is less likely to experience issues with saturation. Spectral bands 1-5, 6(1) low gain, and 7 were stacked to create a multispectral, 30 meter resolution image.

Table 1: Image identification for the 15 Landsat ETM+ scenes used in this analysis

Acquisition Date	Cloud Cover	Path	Row	Landsat ID
12 April 2011	16%	43	34	LE70430342011166EDC00
15 June 2011	0%	43	34	LE70430342011182EDC00
01 July 2011	0%	43	34	LE70430342011182EDC00
17 July 2011	3%	43	34	LE70430342011198EDC00
02 August 2011	0%	43	34	LE70430342011214EDC00
18 August 2011	1%	43	34	LE70430342011230EDC00

03 September 2011	1%	43	34	LE70430342011246EDC00
19 September 2011	0%	43	34	LE70430342011262EDC00
21 October 2011	3%	43	34	LE70430342011294EDC00
24 December 2011	0%	43	34	LE70430342011358EDC00
09 January 2012	0%	43	34	LE70430342012009EDC00
26 February 2012	1%	43	34	LE70430342012057EDC00
30 April 2012	9%	43	34	LE70430342012121EDC00
01 June 2012	0%	43	34	LE70430342012153EDC00
17 June 2012	0%	43	34	LE70430342012169EDC00

A digital elevation model (DEM) was obtained from the USGS National Elevation Database at a spatial resolution of 1 arcsecond (30-meter precision). The DEM is used to adjust surface temperature in order to differentiate cooling effects of elevation from those caused by high rates of ET. Additionally, the DEM is used to calculate pixel slope and aspect – which is used to adjust solar radiation to account for the relationship between intercepted extraterrestrial radiation and radiation at the land surface. Total daily wind run was calculated from 15-minute resolution wind speed data, obtained from a local weather monitoring station operated by the Grasslands Water District within the study area. The wind run grid was used alongside surface roughness to calculate the friction velocity and aerodynamic resistance to heat transport. Frictional velocity and aerodynamic resistance determine sensible heat flux, which, coupled with net radiation and ground heat flux, close the surface energy balance and determine the residual energy partitioned to latent heat flux (converted into instantaneous ET).

The actual radiant energy available at the ground surface is the energy flux density of net incoming radiation (R_n): $R_n = (1 - \alpha)R_{s\downarrow} + R_{L\downarrow} - R_{L\uparrow} - (1 - \varepsilon_0)\, R_{L\downarrow}$; where $R_{s\downarrow}$ is the incident shortwave radiation (W/m^2); α is the surface albedo coefficient (dimensionless); $R_{L\downarrow}$ is the incident longwave radiation (W/m^2); $R_{L\uparrow}$ is the emitted outgoing longwave radiation (W/m^2); and ε_0 is the thermal emissivity of the surface (dimensionless). $(1 - \varepsilon_0)\, R_{L\downarrow}$ represents the reflected fraction of incoming longwave radiation. ReSET builds upon the original energy balance algorithms established by SEBAL (Surface Energy Balance Algorithm for Land). Both ReSET and SEBAL rely on the surface energy balance equation to calculate evapotranspiration estimates (Bastiaanssen *et al*., 1998 a,b; Tasumi *et al*., 2004): $R_n = H + \lambda E + G$; where R_n is the energy flux density of net incoming radiation (W/m^2); H is the flux density of sensible heat into the air

(W/m^2); λE is the flux density of latent heat into the air (W/m^2); and G is the heat flux density into the ground surface (W/m^2).

This method of estimating evapotranspiration based on the energy balance relies on the fact that evaporation and transpiration consume energy. Net radiation is then partitioned to sensible heat flux (H), emitted by atmospheric transport; latent heat flux (λE), emitted by evaporation or transpiration; and ground heat flux (G), absorbed by convection through porous media (Allen *et al*., 2007; Allen *et al*., 2010). Evapotranspiration is transformed from the original latent heat flux estimate (λE) by expressing the water loss as depth of water lost per unit time. The instantaneous evaporative rate is calculated as: $ET_{inst} = 3600\ LE / \lambda$; where ET_{inst} is the rate of instantaneous ET (mm/hr); 3600 is the conversion factor from seconds to hours; and λ is the latent heat of vaporization, estimated as: $\lambda = (2.501 - 0.00236\ (T_s - 273)) \cdot 10^6$; where T_s is the surface temperature (°C).

Ground heat flux is estimated from the sum of net radiation as the ratio between net radiation and heat convection into the soil after Bastiaanssen (1995), as: $G / R_n = T_s\ (0.0038 + 0.0074\alpha) \cdot (1 - 0.98\text{NDVI}^4)$; where T_s is the surface temperature (°C); α is the surface albedo coefficient (dimensionless); and NDVI is the Normalized Difference Vegetation Index (dimensionless). Sensible heat flux is estimated using a one-dimensional, aerodynamic, temperature gradient-based equation for heat transport, as: $H = (\rho \cdot c_p \cdot dT) / r_{ah}$; where ρ is the air density (kg/m^3); c_p is the specific heat of air (1004 J/kg/K); dT is the temperature difference between two heights (°K); and r_{ah} is the aerodynamic resistance to heat transport (s/m). Air density is calculated using mean atmospheric pressure and universal gas law, simplified for the effect of vapor pressure, after Allen *et al*. (1998), as: $\rho = 1000\ P / (1.01(T_s - dT)R)$; where P is the mean atmospheric pressure; R is the specific gas constant (287 J/kg/K); T_s is the pixel surface temperature value (°K); and dT is the near-surface air temperature gradient. Because this formulation of sensible heat flux requires the simultaneous solution of two unknowns (temperature gradient and aerodynamic resistance), two anchor pixels per image are used to solve for the temperature gradient that satisfies the equation given set values of aerodynamic resistance (internally calculated by model) and wind speed (field-based data).

These pixels were chosen by querying the elevation-adjusted ground temperature image for representative maximum and minimum values. The hot pixel represents an area where no evapotranspiration is occurring (and consequently, no or minimal energy is lost to sensible heat flux associated with the change of state of water during evapotranspiration). The cold pixel represents an area of high ET and, depending on site conditions, may either fall in open water (water surface evaporation exceeding evapotranspiration) or in heavily transpiring vegetation patches (ET exceeding water surface evaporation). A linear relationship between surface temperature and dT is based on the two discrete known surface temperature points and temperature gradients. The temperature gradient satisfying the sensible heat flux equations is calculated as: $dT = a \cdot T_s + b$; where T_s is the pixel surface temperature (°K); $a = (dT_{hot} - dT_{cold}) / (T_{s,hot} - T_{s,cold})$; and $b = dT_{hot} - a \cdot T_{s,hot}$.

Aerodynamic resistance is estimated assuming neutral atmospheric stability, as: $r_{ah} = \log_e (z_2 / z_1) / (u^* \cdot k)$; where z_1 and z_2 are the heights above the zero plane displacement of vegetation (m); u^* is the frictional velocity due to turbulence fluctuations in the air (m/s); and k is von Karman's constant (0.41). The frictional velocity is calculated using the logarithmic wind law for neutral atmospheric conditions, as: $u^* = (k \cdot u_x) / (\log_e (z_x / z_{om}))$; where k is von Karman's constant; u_x is the wind speed at height z_x (m/s); and z_{om} is the momentum roughness length (m). This iterative approach using anchor pixels calibrates the sensible heat flux calculations.

Surface temperature was derived in ReSET as a function of NDVI (Normalized Difference Vegetation Index), surface albedo, topography, and the Landsat thermal band as shown in the ReSET ground (surface) temperature workflow (Figure 2). NDVI is used to estimate thermal emissivity by mapping the distribution and density of green vegetation per image pixel, and is calculated as: $NDVI = (\rho_{t,4} - \rho_{t,3}) / (\rho_{t,4} + \rho_{t,3})$; where $\rho_{t,4}$ and $\rho_{t,3}$ are the at-satellite reflectance value of bands 4 and 3, respectively. Surface albedo is calculated as the ratio of reflected radiation (from the surface) to the incident (i.e., incoming) shortwave radiation (at the surface). Albedo is a single value which combines the reflectance values of bands 1-5 and 7. Surface temperature is calculated using a modified Plank equation, as: $T_s = K_2 / (\log_e((\varepsilon_{NB} \cdot K_1 / R_c) + 1))$; where T_s is the pixel surface temperature (°K); ε_{NB} is the "narrow band" surface emissivity of Landsat band 6 (dimensionless); R_c is the adjusted thermal radiance from the surface

(W/m^2/sr/μm); and K_1/K_2 are thermal band constants used to calibrate the conversion of spectral radiance to temperature, parameterized for Landsat ETM+ imagery after Chandler *et al*., 2009 (W/m^2/sr/μm).

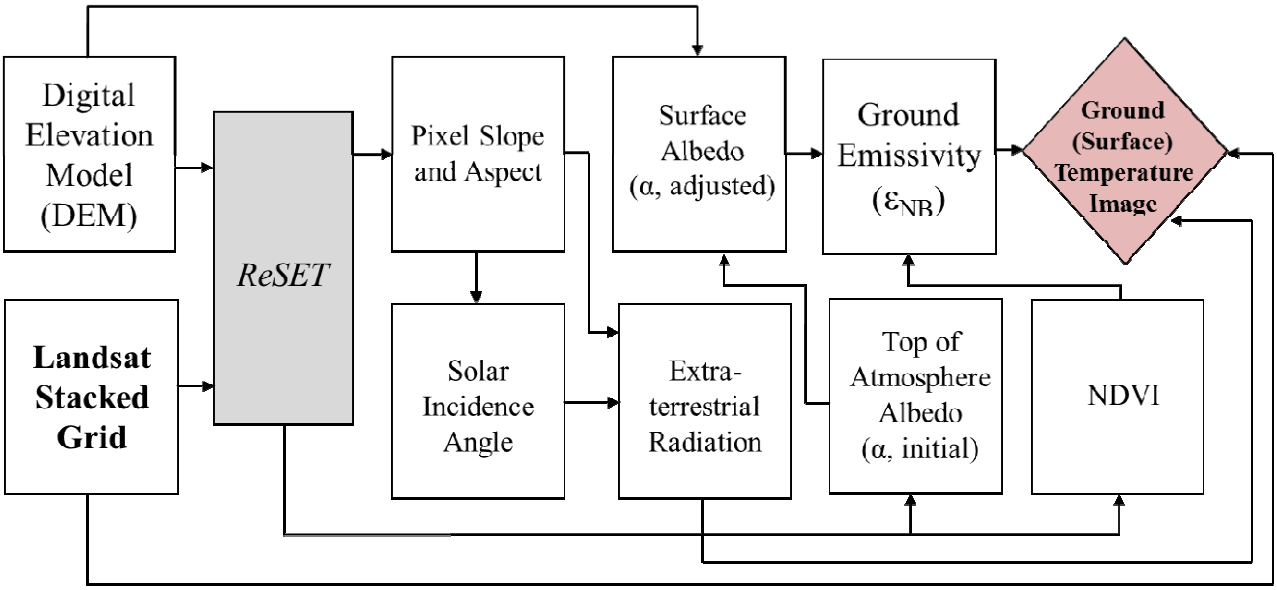

Figure 2: ReSET conceptual model, showing work-flow for the calculation of a spatially-distributed grid of surface temperature from the raw Landsat ETM+ image. The DEM and Landsat image are inputs into the ReSET model; initial outputs (i.e. top of atmosphere albedo, NDVI) become inputs at subsequent steps. The ground surface temperature image is processed further (see Figure 3) to delineate the wetland footprint by classifying wetland areas into zones of flooded and dry emergent vegetation.

2.3. *Classification and Signal Processing*

Once a grid of surface temperature is derived, it must be post-processed and classified in order to draw meaningful conclusions about changes in the wetland "footprint." A multispectral band combination was created from the raw Landsat image to convert the continuous float data into a thematic raster. A band ratio of bands 5 (mid-infrared, 1.55 – 1.75 μm) and 2 (green, 0.52 – 0.60 μm) was found to provide adequate classification of the study area into the three principal categories of interest: open water, wetland and upland. Following preliminary classification into a 3-class processed band ratio (Figure 5) - the wetland class was further subdivided into flooded and terrestrial vegetation classes. The classification of vegetation based on standing water presence (flooded), or its absence (terrestrial), was accomplished by testing the validity of the

proposed hypothesis that presupposed discernible surface temperature differences could be distinguished despite the presence of vegetation.

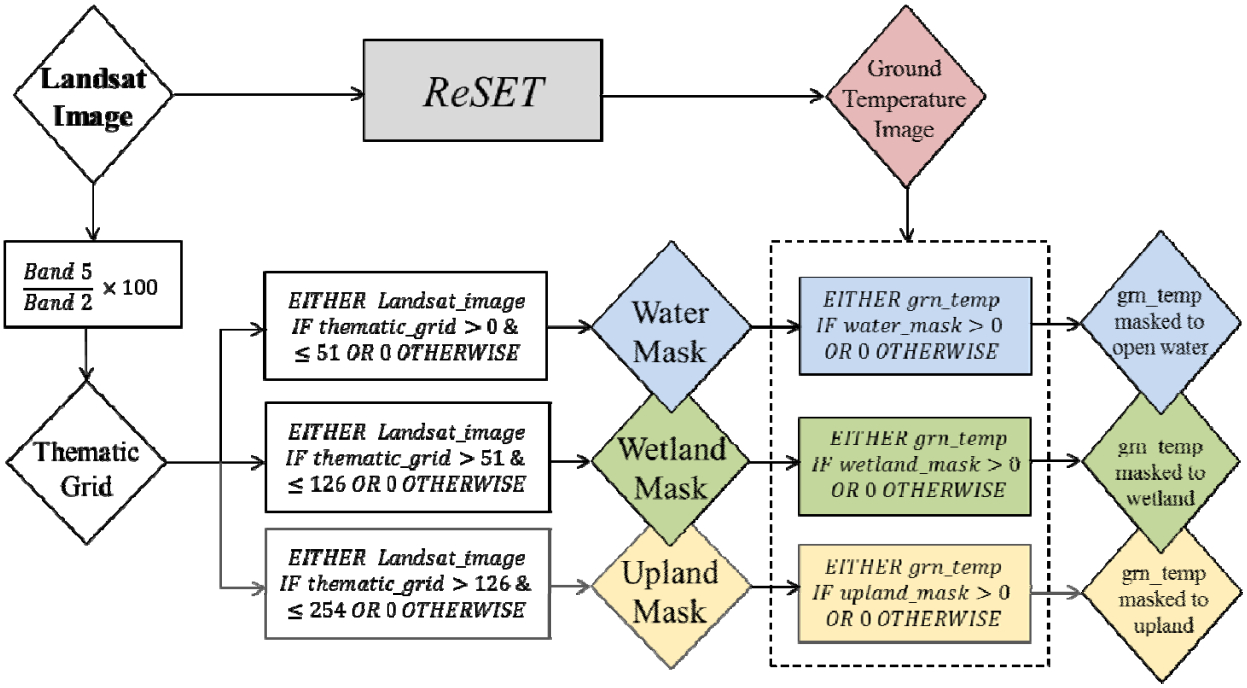

Figure 3: Initial classification workflow, represented using structure and syntax analogous to that used by ERDAS Imagine model builder. First, the Landsat image is converted into a thematic grid via a band ratio transformation. Thresholds (see Table 2) are applied to extract pixels which correspond to open water, wetland, and upland land cover types. These images are used to "mask" the ground temperature image (imported from ReSET – see Figure 2), and are used as inputs for the next classification workflow (Figure 4).

Unsupervised classification clusters pixels into a predetermined number of classes based on image statistics and operator-defined threshold parameters. The method is less susceptible to operator bias, but can generate classes that are difficult to interpret. Supervised classification can provide the operator with the ability to distinguish between categories that do not have clearly differentiable spectral signals, but may create classes which are forced or artificial. Unsupervised classification assigned pixels to a set number of classes by iteratively changing the mean and standard deviation of each class, as newly assigned pixels changed the statistical makeup of the group – forcing previously assigned pixels to become reassigned. Fewer classes inherently produce larger standard deviations within each class, and subsequently, the potential for greater numbers of pixels to be incorrectly categorized by the operator. Furthermore, unsupervised classification produces groups based on a statistical relationship to the input; clusters represent groups of largely self-similar pixels, but do not necessarily translate to the expected classification

scheme. While this may be problematic in terms of classifying a certain set of groups, it serves as a highly useful and unbiased litmus test for whether thermal properties produce a discernible signal to map the wetland footprint (as proposed). Running unsupervised classification for a larger number of classes produced classes with smaller deviations, increasing the likelihood of self-similarity and decreasing the likelihood of misclassification. However an increased number of classes did not directly translate into a proportional increase in the number of expected categories. Subsequently the final unsupervised classification of surface temperature was limited to two classes.

The ReSET ground temperature image was masked to include only the wetland pixels - effectively removing all open water and upland cells. The wetland-bounded ground temperature pixels within the Area of Interest were classified using unsupervised classification and the

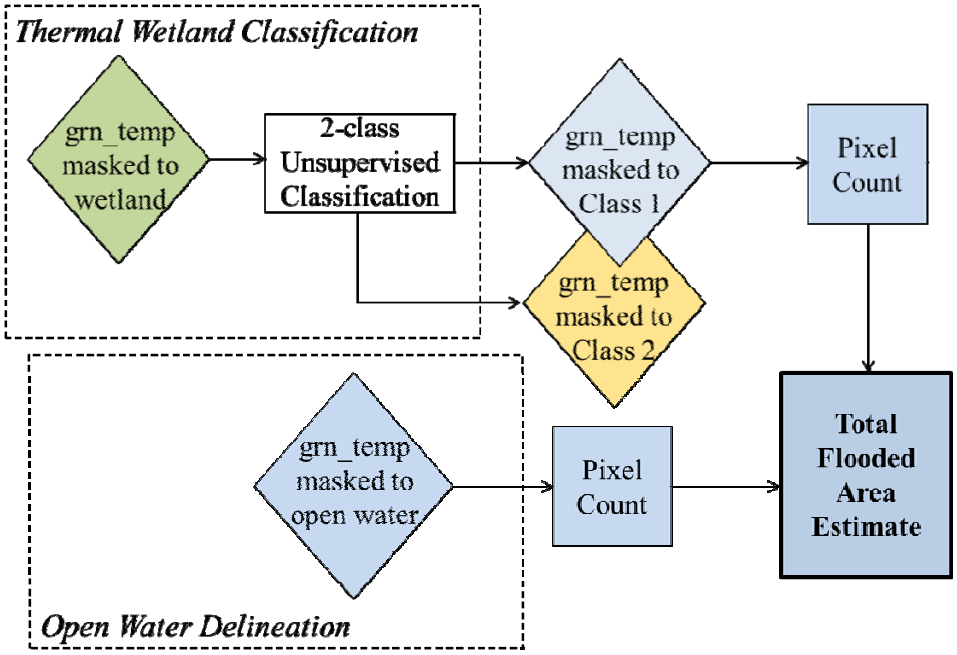

Figure 4: Secondary classification workflow, showing the procedure for classifying the wetland into inundated (Class 1) and dry (Class 2) zones based on the thermal signal (imported ground temperature image – see Figure 3). Together with pixels classified as inundated wetland, open water pixels form an aggregated estimate of total flooded area. Upland pixels (see Figure 4) are assumed to contain no standing water and are excluded from the wetland footprint.

Iterative Self-Organizing Data Analysis technique (ISODATA). Classification was carried out for two classes (categories of interest: Wetland Class 1 – flooded, and Wetland Class 2 –

terrestrial) with the following settings: 50 maximum iterations; 0.999 convergence threshold; and the classification initialized from statistics. In this study, the term 'categories of interest' is used to distinguish between the raw results of the classification and the categories into which the operator assigns the output.

GIS-based wetland pond stage-surface area and stage-volume relationships have been previously developed for twelve instrumented ponds within the wetland complex. The ponds formed part of a four year (2006-2009) experiment to investigate the effects of modified drawdown regimes on SJR wetland ecosystem services and habitat quality. Ponds were chosen to cover the majority of wetland types within the study area; representing a range of vegetation and soil types, average salinity, pond depth, and inflow and outflow sources. Each was instrumented with flow and water quality sensors logging continuous 15-minute resolution data exported by way of a radio/remote telemetry platform (Quinn *et al*., 2010; Rahilly *et al*., 2010). A 2007 GPS survey of the ponds produced bathymetry maps from which stage-surface area and stage-volume relationships were calculated. The GPS data were logged using ATV-mounted Trimble GPS surveyor-grade units which provided a vertical accuracy to within 0.1 feet (0.03 meters). Presently, only four of the original twelve ponds remain in the monitoring program. ESRI ArcGIS Spatial Analyst software was used to develop a three-dimensional model of each surveyed wetland pond. The three-dimensional rendering was divided at 0.1-foot (0.03-meter) vertical intervals to derive pond-specific relationships between pond surface area and depth, and pond volume and depth (Quinn *et al*., 2010). Depth sensors at these four ponds track pond stage throughout the year. Utilizing continuous stage and flow data - the previously established relationships between (a) pond depth and surface area and (b) between pond depth and volume - produced an adequately robust estimate of daily pond surface area. Classification results were curated and validated against corresponding depth-surface area data sets at two control ponds within the study area – Ducky Strike Club north field, and Mud Slough Unit field 3b, and statistically analyzed to estimate variance and test for group independence.

The two control ponds at the Ducky Strike Duck Club and Mud Slough Wildlife Management Area provided benchmark surface areas (converted to a pixel count - where 1 Landsat pixel = 900 m^2) estimates against which post-classification sums of open water and flooded vegetation

results could be compared. While this approach could determine error margins and the under or overestimation of total flooded area, it was not spatially distributed. In other words, it provided no information on the accuracy of individual pixel assignment to a given classification class.

3. Results and Discussion

A series of 15 Landsat ETM+ images was analyzed using ERDAS Imagine and ReSET. For the purposes of water resource management, a water year begins on September 1st of one calendar year, and ends on August 31st of the following calendar year. A longer timeframe, spanning April 12th, 2011 – June 17th, 2012, was analyzed in this study (see Table 1). This decision was made with the intent to provide the foundation for subsequent inter-annual comparison, as well as to generate a denser data-set. The complete 15-image dataset is included in the discussion of field-based validation results (Figures 8-9). However, to most intuitively communicate the seasonality of the GEA wetland system, a subset of 9 of the 15 images is presented in Figure 5. Pixels corresponding to area classified as open water are shown in blue. Pixels mapping to terrestrial and emergent vegetation patches are shown in shades of light and dark green, respectively. The classified results of the bands 5 and 2 transformation show the cyclical nature of seasonal wetland management beginning with the August 2nd, 2011 image (Figure 5a). Subsequent images capture the progression of fall flood-up, then the winter period at maximum pond "shooting" depth, followed by spring pond draw-down.

The ponds start to fill during late August 2011 (captured in the satellite's overpass on August 18th) and continue during September 2011. The open water area increases significantly between the September 3rd, 2011 and September 19th, 2011 satellite overpass. By October 21st, 2011 flood-up is largely complete. The flooded surface area remains static throughout the months of December, January, and February to provide wintering habitat for wildfowl. Pond drawdown is first captured in the February 26th, 2012 image. At this point, the effects of initial wetland releases on the wetland footprint first become discernible (Figure 5h). Drawdown continues through the spring, approaching completion by April 30th, 2012. Few ponds remain flooded and wetland grasses appear in some of the drained areas (Figure 5i). Depending on water availability from the Central Valley Project, one or more irrigations during the summer are used to sustain soil moisture and maximize vegetation biomass and seed production. Most of the irrigation water

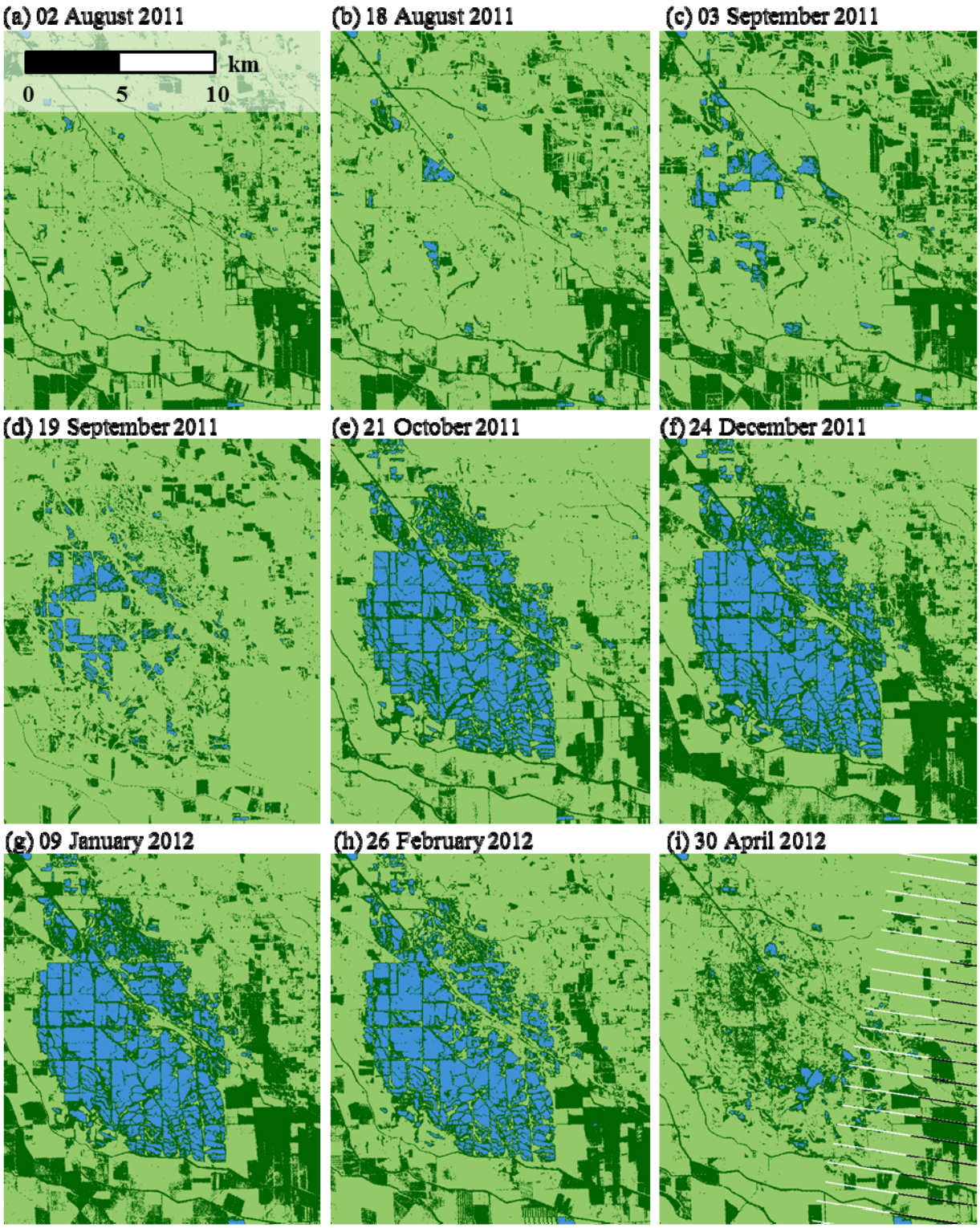

Figure 5: Classified output from multispectral band combination, showing thresholds (see Table 2) applied to the output of the Band 5 to Band 2 ratio. Open water is shown in blue, wetlands in dark green, and uplands in light green. The full Landsat ETM+ image is shown clipped to the south Grasslands Ecological Area.

deep percolates. Any remainder is discharged to Mud or Salt Slough through the same network of drainage canals that conveyed the primary pond drawdown volume.

3.1. *Procedure for Delineating Flooded Area*

The band ratio-based classification shown in Figure 5 captured not only the progression of flood-up and the consequent change in open water surface area, but also seasonal fluctuations in moist soil vegetation (shown in dark green) relative to the combined terrestrial vegetation and bare ground surface area classified as upland (light green). This band ratio is similar to one formulation of the Normalized Difference Water Index, in that both use the signal from mid-IR and visible green wavelengths (NDWI = $(\rho_{t,5} - \rho_{t,2}) / (\rho_{t,5} + \rho_{t,2})$; where $\rho_{t,5}$ and $\rho_{t,2}$ are the at-satellite reflectance value of bands 5 and 2 (Allen *et al.*, 2010)). Bands 5 and 2 are sensitive to water absorption (moisture content) and green vegetation reflectance, respectively. By contract, NDVI uses a ratio of bands 3 and 4 (visible red / near IR), which are sensitive to chlorophyll concentrations and plant tissue structure, respectively. The availability of sufficient field-derived spatial data can make delineating the boundaries between wetland and upland vegetation easier to accomplish by establishing some initial spatial constraints on the wetland pond area. The mid-IR to green (5:2) band ratio circumvents the need to define the spectral signatures of emergent wetland vegetation. The combination of visible green and mid-infrared wavelengths made for an efficient preliminary classification tool which effectively combined the ability to map both the presence of vegetation (measured by NDVI) and the water content (measured by NDWI).

Vegetation indices, such as NDVI, are sensitive to climatic (Roerink *et al.,* 2003; Pettorelli *et al.*, 2005; Mänd *et al.*, 2010) and plant physiologic controls; particularly those corresponding to plant health (Thelen *et al.*, 2004, Ortiz *et al.*, 2011). Atmospheric conditions, such as the concentration of aerosol particles emitted from anthropogenic sources or as a result of wildfires, also influence NDVI (Holben, 1986; Gao,1996; Xiao *et al.*, 2003). Unlike the near-instantaneous change in temperature corresponding to the phase transformation of water to vapor, NDVI displays a delayed response to water availability. The time lag between increased moisture (via any combination of precipitation, irrigation, or exfiltration fluxes) and plant response has been shown to range from two months (Richard and Poccard, 1998) to fewer than five days (Wang *et*

al., 2007). Eklundh (1998) found statistically significant time lag periods difficult to establish, concluding that consistency may be region-dependent. Others found seasonality to play a governing role (Ji and Peters, 2003; Piao *et al.*, 2006). In short, factors other than standing water availability are capable of affecting the NDVI thresholds between wetland and terrestrial vegetation. This sensitivity to non-control (presence standing water) variables would have required adjustment for long-term analysis and delineation from Landsat images acquired over multiple months, seasons or water years. Conversely, the 5:2 band ratio thresholds were kept constant for all 15 images and the accuracy of this static classification scheme showed no bias toward certain images or seasons. While this ratio provides less detailed information about plant health, and may not be adequate for finer-resolution classification of plant communities, it is well-suited to the objectives of this study with their primarily hydrologic, rather than ecological, focus.

3.2. *Multiband Transformation for Water, Wetland, and Upland Delineation*

Band ratio classification approaches were used to manipulate multispectral images and reduce the variability of a single-band signal, such as those caused by variations in atmospheric or topographic conditions (Xu, 2006). Typically, the pixel's digital number (DN) in one spectral band is divided by the analogous DN in another spectral band. Although this procedure degrades the overall signal by stripping a pixel of the DNs of the remaining bands, it tends to accentuate more faint spectral variations, and attenuate much of the background noise associated with different wavelength regions (Li *et al.*, 2009).

The Landsat ETM+ 5:2 multiband transformation calculates the ratio of mid-infrared (mid-IR) to visible green wavelengths and multiplies the output by 100 to convert the continuous (float) output to integer values: *Thematic output* = (*Band 5 / Band 2*) x 100; where *Band 5* is the at-satellite reflectance value of the mid-infrared wavelength (1.55 – 1.75 µm, 30-m precision), and *Band 2* is the at-satellite reflectance value of the visible green wavelength (0.552 – 0.605 µm, 30-m precision). This transformation converts the image into a thematic grid of 256 brightness values (integer pixel values: center panel, Figure 6) in the range of 0 to 255. The ratio is generally greater than one (thematic output values > 100) for terrestrial ("upland") pixels, since

there is greater absorption of the visible green wavelength (band 2) in soils and greater reflectance of mid-IR (band 5). Conversely, the ratio is less than one (thematic output values < 100) for water bodies. While water reflects light in the visible spectrum (bands 1-3), in the near- and mid-IR range, more is absorbed. Low vegetation density in open water results in a corresponding decrease in the absorption of the visible green wavelength.

Despite the suitability of the 5:2 band ratio for delineating the land-water interface, the less than 100 versus greater than 100 threshold requires adjustment for coastal delineation in study areas with vegetated banks or inundated vegetation (Alesheikh et al., 2007). In wetlands, or any other system where the area of interest spans a terrestrial-aquatic gradient, there is rarely a sharp demarcation between "no vegetation" and "no water." Inundated emergent vegetation effectively represents a third class, straddling the 100 threshold. Classification thresholds were set after Dobson (2011). Threshold parameters for the classification are listed in Table 1. A graphic representation of the Landsat image post-classification is shown in the right panel (Figure 6).

Table 2: Classification of mid-IR / visible green band ratio output into three preliminary classes.

Classification Category	Threshold
Open Water	1 - 51
Wetland	52 - 126
Upland	127 - 254
No Data	0, 255

The classified image was compared visually against the original Landsat image. The 7,5,3 (RGB) band composite was selected for its effective atmospheric penetration and surface water delineation. This band combination produces a "natural color" image. Vegetation appears in shades of green; urban areas in white or gray; water is dark blue to black depending on depth; and soils are assigned various combination of remaining colors. The images in Figure 6 were clipped from the original Landsat image (170 km north-south by 183 km east-west (106 mi by 114 mi)). Processing was carried out for the entire area encompassing both North and South Grassland Water District (GWD) areas. However the analysis focused on the South Grasslands area (shown in Figures 5-7) for two reasons: 1) the two monitored ponds (discussed later in the results section) are both located in the South Grasslands, and 2) to highlight smaller-scale

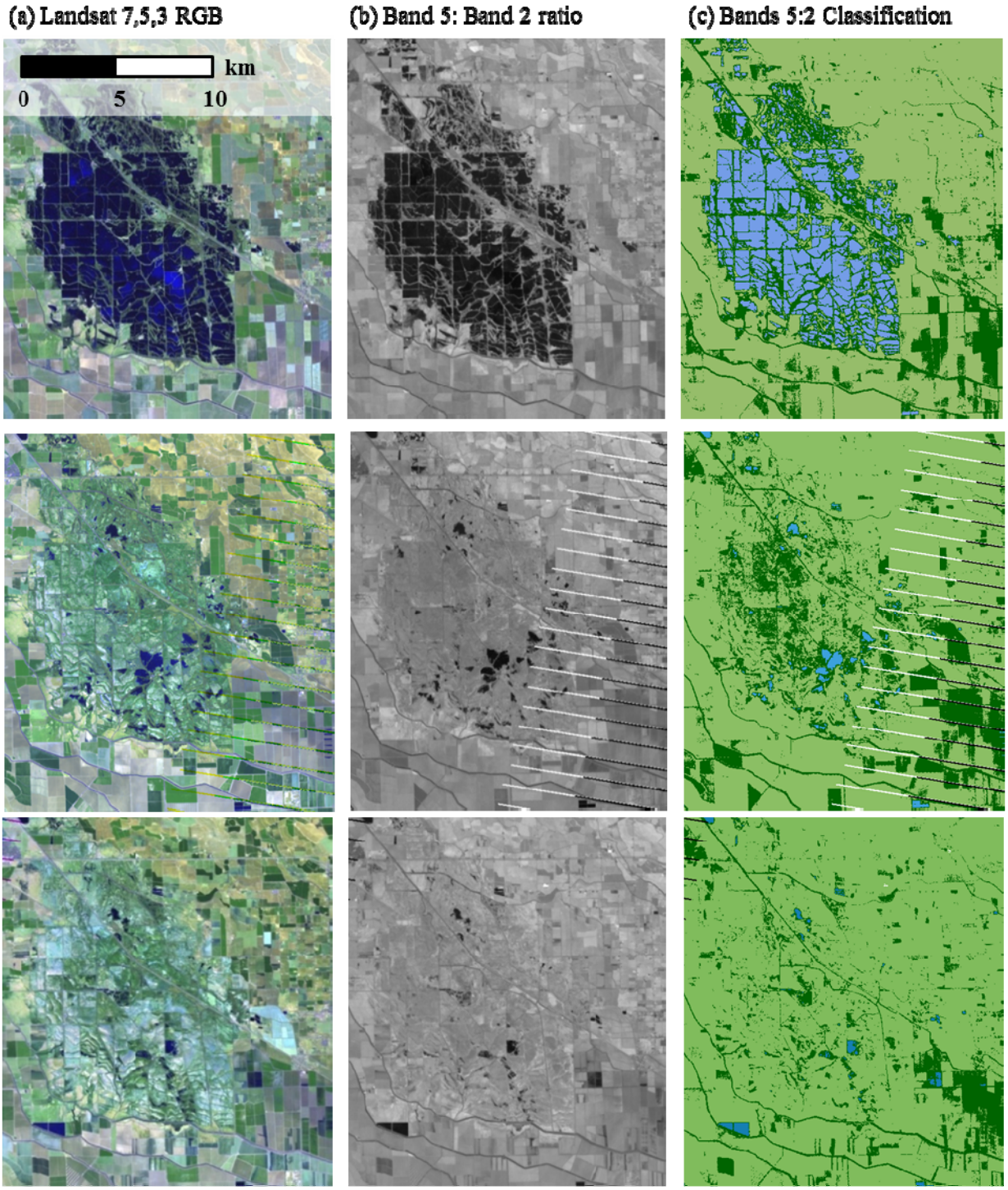

Figure 6: From top to bottom: multiband transformation for South Grassland WD showing seasonal flood-up captured on October 21st, 2011; draw-down captured on April 30th, 2011; and drained ponds at end of flooded season in a scene from June 17th, 2011. From left to right: column (a) Landsat ETM+ image spectral band combination 7,5,3 (R,G,B); column (b) initial output of Band 5/Band 2 ratio; column (c) classification of Band 5/ Band 2 ratio into open water (blue), wetland (dark green), and upland (light green).

features which would have been difficult to distinguish at a coarser resolution. Additionally, the image was intentionally left unclipped to the GWD pond perimeters to illustrate the behavior of wetland and upland mid-IR to green band ratio thresholds when applied without spatially constraining the classification.

The 5:2 band ratio thresholds performed well when tasked with open water delineation. This was evident from comparisons of the original 7,5,3 RGB composite Landsat images (Figure 6, left panel) with the classification results (Figure 6, right panel). Thresholds were set to favor a classification of "wetland" rather than "open water" in cases of ambiguity. This was done deliberately because of the potential impact on the final thermal classification. Introduction of a small number of transitional cells could skew the sample mean towards cooler temperatures and introduce more wetland cells to the class during the unsupervised classification – thereby separating them from upland cells or those with higher proportions of bare soil cover. The wetland/upland transition was more difficult to qualify without empirical data. Upland classification successfully recognized all areas of bare soil as well as drier vegetation patches.

3.3. Comparison with Monitored Control Ponds

Thematic conversion and classification into open water, wetland and upland classes helped to quantify the relative area of open water to the total flooded area. Uplands were ignored during subsequent classification as having insufficient water content to be considered inundated areas and contributing to the total flooded area estimate. The remaining wetland class comprised emergent moist-soil wetland vegetation - which may be flooded and grow in standing water or, depending on vegetation type and time of year, may remain dry land. The results of the classification were compared to two controls. These were (a) a preliminary visual inspection of the 7,5,3 Landsat image (Figure 7: a-b,e); and (b) comparison with existing elevation-surface area bathymetry relationships for two ponds (Ducky Strike Club North Field - Figure 7: b-d) and Mud Slough Unit Field 3b - Figure 7: e-g) that were continuously monitored, using YSI 650XL sondes, for stage, flow and electrical conductivity. The colder ground temperature class (Figure 7: d,g) was assigned to flooded vegetation and the warmer ground temperature class to terrestrial

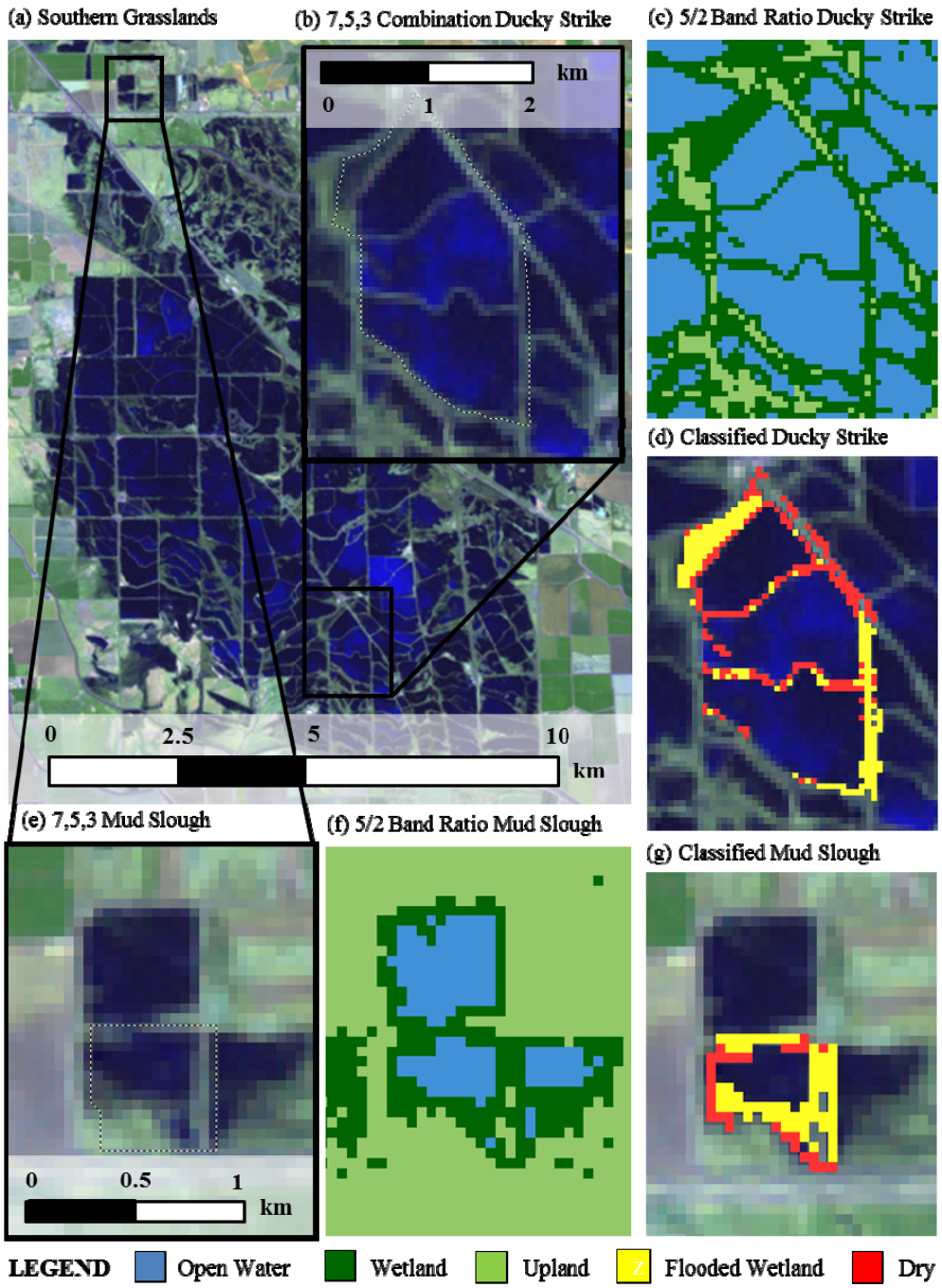

Figure 7 (a-g): Central image (a) showing the multispectral band combination of the original Landsat image, clipped to the south Grassland Ecological Area. Insets (b) and (e) show the two validation sites – the Ducky Strike Club north and Mud Slough 3b wetland units, respectively. The initial Band 5/Band 2 ratio classification – shown in (c) and (f), partition the image into open water, wetland, and upland categories. The results of unsupervised classification of surface temperature – shown in (d) and (g), delineate the boundary between flooded and dry wetland vegetation. The extent of the "wetland footprint" is captured by open water and flooded wetland area.

vegetation, based on the expected temperature response to the presence of water and the effect of evaporative cooling.

A comparison of open water surface area (Figures 8-9: blue) to the total flooded area (Figures 8-9: green) calculated for the two continuously monitored control ponds (DSN and MS3b) showed the contribution of flooded wetland vegetation to the total flooded area. This additional flooded area, covered by wetland vegetation, was underestimated by analysis limited to open water classification. At the Ducky Strike Club (Figure 8), the attempt at wetland open water delineation for the north field underestimated the full extent of flooded surface area by as much as 38% during flood up, whereas underestimation was reduced to 8% using the combined open water and flooded wetland classification. During the entire duration of flood-up captured in Landsat images (October 21st, 2001 through February 26th, 2012), open water delineation at DSN underestimated 311 pixels of total flooded area (equivalent to a surface area of 279,900 m^2). In contrast, 40 pixels (36,000 m^2) were overestimated using the proposed combination of classified flooded wetland and open water. At Mud Slough Unit field 3b (Figure 9), the open water analysis resulted in flooded area underestimates of up to 63% relative to monitored - however with the addition of thermal wetland classification to the total flooded area estimation - this error was reduced to 13%.

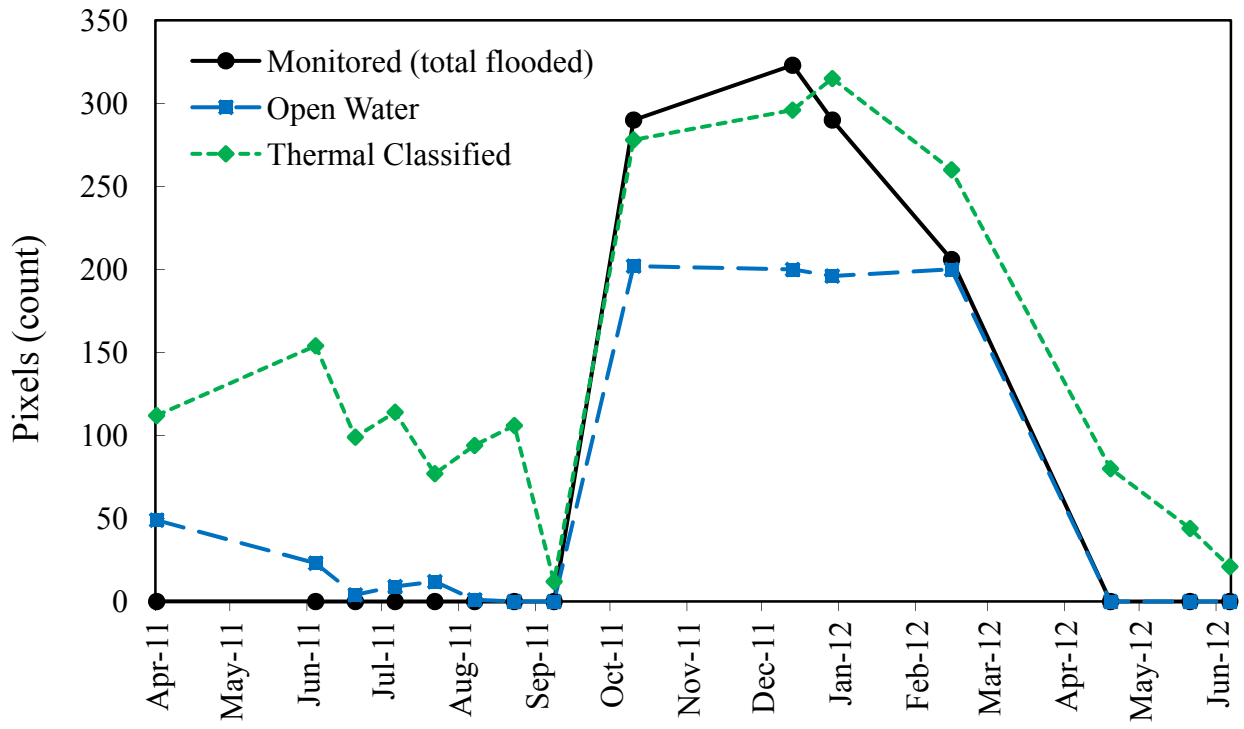

Figure 8: Results of field-based validation at the Ducky Strike Club north pond. The monitored total flooded area (solid black) is plotted against the area of the "wetland footprint," as derived using the proposed classification scheme, where Thermal Classified = Open Water + Wetland Class 1. This estimate is compared to the extent of open water – illustrating the underestimation of total inundated area. Surface area is shown in units of pixels: one Landsat ETM+ pixel is equivalent to 900 m^2.

While the thermal classification performed similarly during the flood-up period, the accuracy of the wetland land use delineation differed between the two control ponds during both wetland flood-up and spring drawdown. In MS3b (Figure 9) a largely bimodal pattern was evident over the course of the year – the pond filled rapidly to the maximum flooded area. Drainage was also rapid – the drawdown period was captured during the time interval of a single satellite image. This pattern was replicated for the changing open water surface area. Estimates from the preliminary band ratio classification, which assigned open water a mid-IR/green visible wavelength ratio value of 1-51 (Table 1), remained near zero during periods of drawdown.

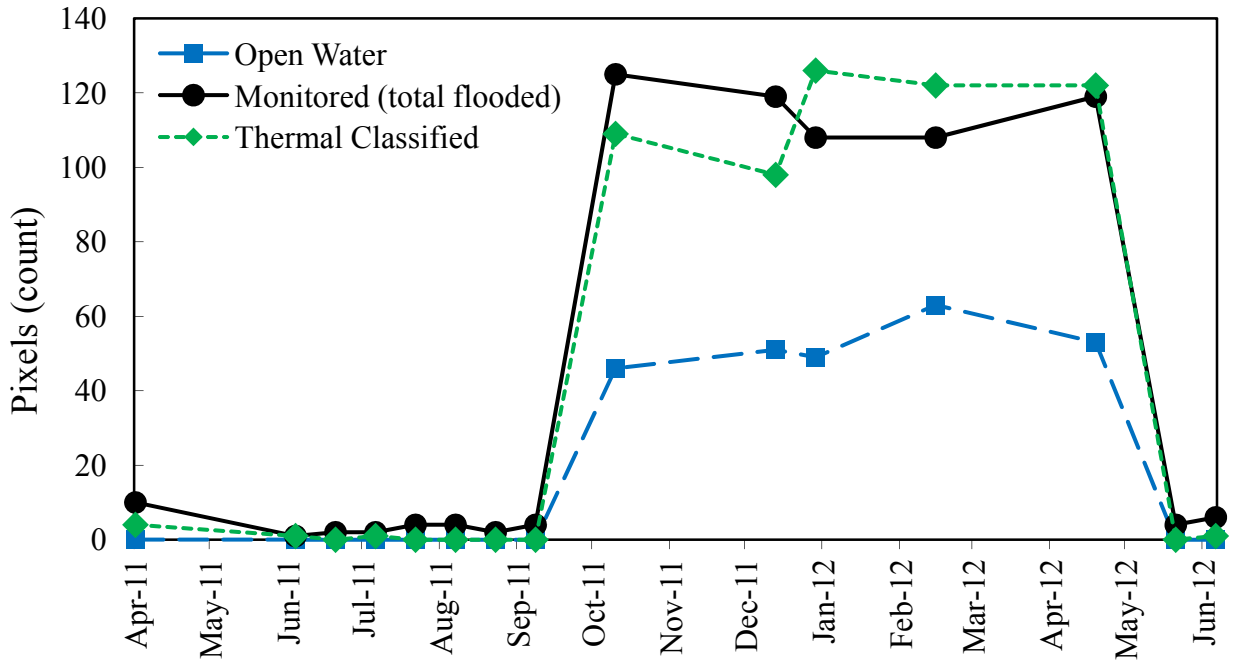

Figure 9: Results of field-based validation at the Mud Slough 3b pond. The monitored total flooded area (solid black) is plotted against the area of the "wetland footprint," as derived using the proposed classification scheme, where Thermal Classified = Open Water + Wetland Class 1. This estimate is compared to the extent of open water – illustrating the underestimation of total inundated area. Surface area is shown in units of pixels: one Landsat ETM+ pixel is equivalent to 900 m^2.

While the rate of change in open water during wetland flood-up (September 19th – October 21st) and wetland drawdown (April 30th – June 1st) mirrored similar changes in monitored total flooded area – reliance on open water surface areal delineation underestimated the total extent of flood-up (black– Figure 9). This was obtained by unsupervised classification of wetland surface temperature. At DSN (Figure 8), open water surface area began to decrease half-way through the flood-up period (obtained by classification and validated by monitoring data), and drawdown rate was shown to be more gradual. Open water delineation replicated the slope of monitored total flooded area on both the rising (flood-up) and falling (draw-down) limbs. The time lapse between combined flooded vegetation and open water estimates and the monitored dataset (peaks on January 9th versus December 24th, respectively) and overestimation by thermal classification at DSN during wetland drawdown can be attributed to a lagging vegetation response to changing water availability. This pattern was not replicated at MS3b due to the significantly more rapid wetland drawdown. The results of thermal classification at DSN also significantly overestimated flooded area during summer months, when the addition of cooler (class 1) wetland area increased

total flooded surface area estimates - and the magnitude of error relative to monitored data, to nearly 50% of area at max flood-up. For applications in managed wetlands, this overestimate can be avoided by limiting the addition of cooler wetland area to the open water total only during the flood-up period.

Total flooded area was better approximated using a combination of open water delineation and surface temperature classification of the wetland class, with significant improvement in flooded surface area estimates relative to previous open water delineation at two control ponds during the seasonal flood-up period. Additional refinement – through a combination of finer resolution imagery, subpixel classification techniques, or by increasing the number of initial unsupervised classes followed by post-classification merging of self-similar polygons, was expected to further reduce both under and overestimates during flood-up. In seasonally managed wetlands, a priori knowledge of the system can be used to constrain the flood-up period. Such temporal constraints would be used to limit the flooded wetland classification to periods of pond flooding and eliminate the significant overestimation caused by the erroneous addition of wetland area at DSN (Figure 8).

3.4. Effect of Standing Water Availability on Mean Surface Temperature and Variance

Within the available dataset, differences in surface temperature variance correspond to larger extent to changes in sample size rather than represent inherent physical differences between open water, flooded and terrestrial wetland vegetation, or uplands. Open water would be expected to show the smallest variance, as it represents the single most homogenous class and the classification is spatially constrained to a single pond to control for the effects of topography and dissimilar management. Conversely, the variance of open water surface temperature was significantly higher during full flood-up – an order of magnitude greater than the variance of all other classes (October 21st – January 9th, Table 2) when the wetland footprint was approaching or at its maximum and open water population exceeded all other classes. During spring drawdown (April 12th – Table 2), as managed drainage began to transition the pond area from fully flooded to dry, the difference between open water and other classes' variances narrowed, reflecting changing standing water availability and a greater number of dry pixels.

During the process of flood-up in the fall (21 Oct 11, Figure 11a) and the progression of draw-down in the spring (12 Apr 11, Figure 11b), mean open water surface temperature noticeably exceeded the means of wetland and upland temperatures. Net radiation (R_n) partitioned to heat flux into the water (G) during warmer months created a thermal sink. Once decreased air temperatures in the fall and winter reversed the potential drop, water was transformed into a thermal source. In winter, late fall, and early spring this energy, stored as heat, was lost to sensible heat flux (Allen and Tasumi 2005).

Overall, the Open Water class had the least variance across spatial and seasonal . The comparatively lower Open Water surface temperature mean was attributed to the effect of heat flux G into the water. The difference in air and water surface temperature created a thermal potential drop during summer months that was directed into the water column - which acted as a thermal sink, rather than into the atmosphere (thermal source). While the presence of vegetation damped the potential to partition R_n to G (less water per unit area), the addition of transpiration to evaporative potential most likely contributed the additional cooling, and accounts for differences between Open Water and Wetland Class 1 mean surface temperature for the three summer Landsat images in Figure 10.

(a) 01 Jul 11 Ducky Strike North Field

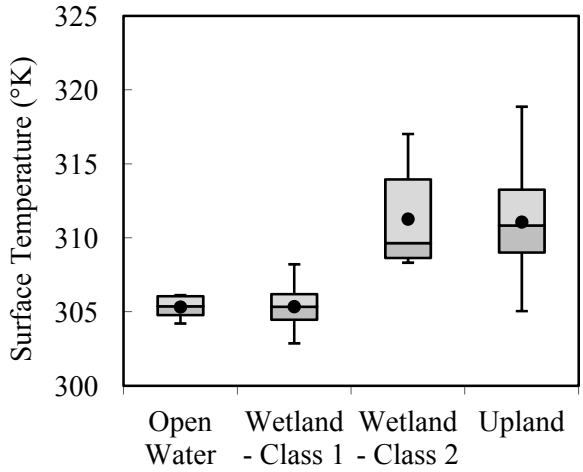

(b) 17 Jul 11 Ducky Strike North Field

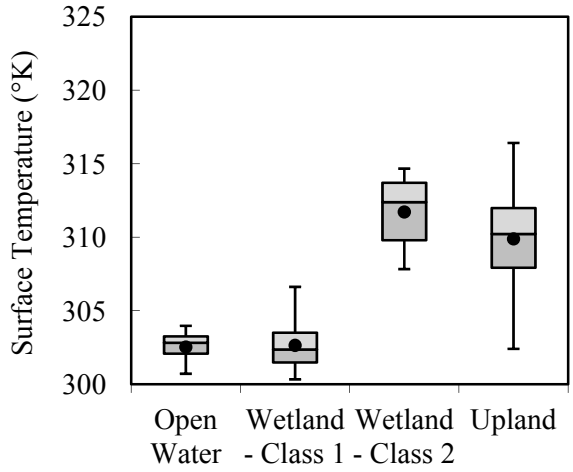

(c) 02 Aug 11 Ducky Strike North Field

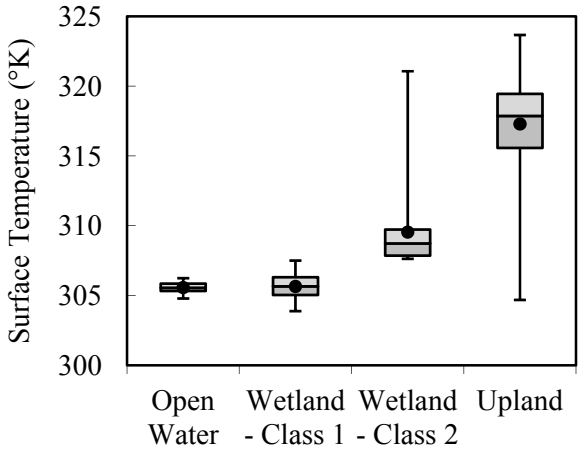

Figure 10 (a-c): In July and August, the mean open water surface temperature was substantially lower than that of upland areas, and marginally but consistently lower than the Wetland Class 1 temperature. Within the wetland category, Wetland Class 1 had a mean temperature similar to the mean open water surface temperature - despite the greater variance within the Class 1 wetland category, due to a larger wetland population during summer months when ponds experience draw-down.

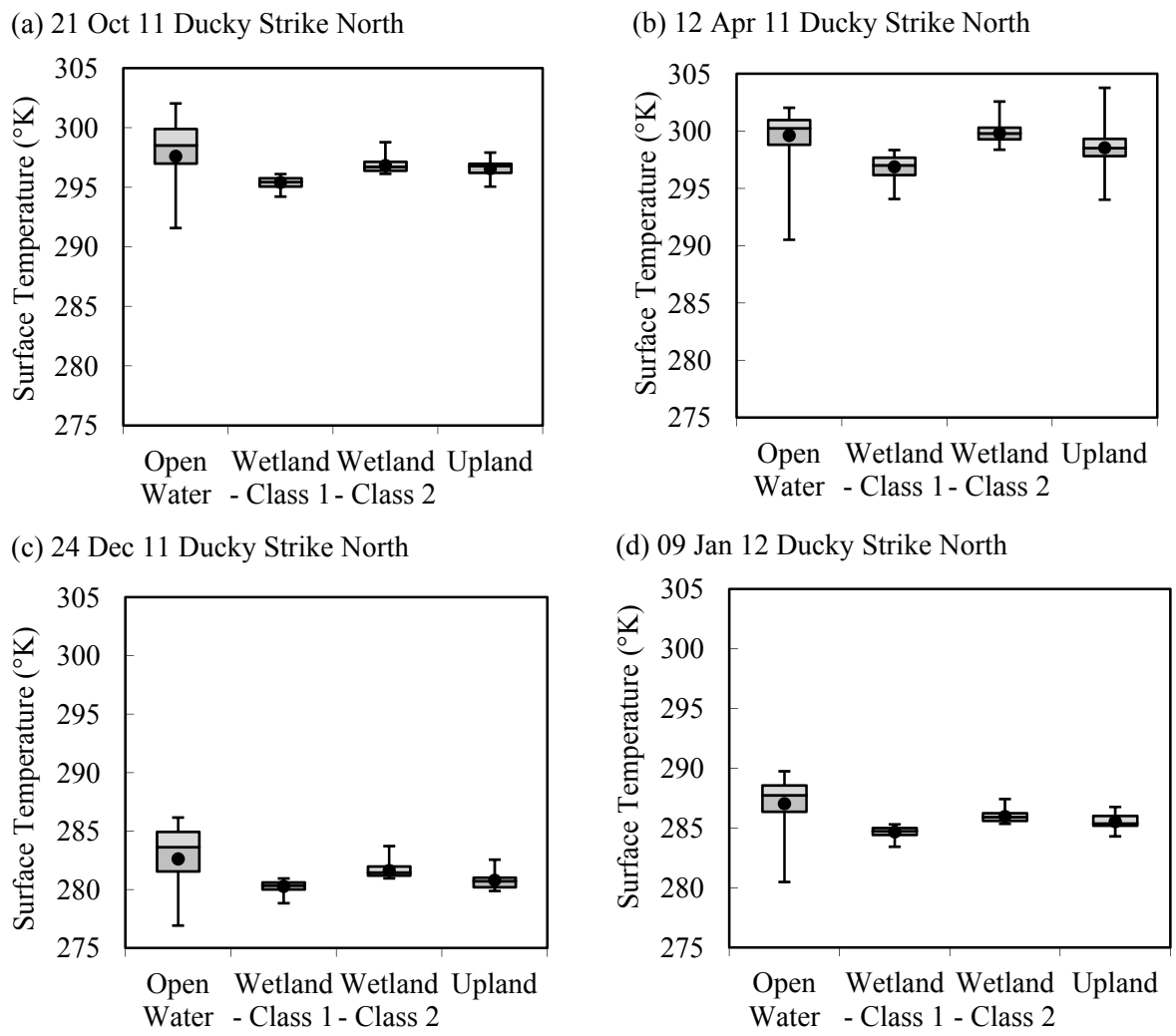

Figure 11 (a-d): Surface temperature plots for four months capturing the fall flood-up and spring draw-down periods. Mean surface temperature was highest for the open water class across all four groups.

Table 3: Ducky Strike Club north pond - surface temperature variance (ºK) across four Landsat satellite image acquisition dates capturing full flood-up (Oct 21st, 2011 – January 9th, 2012) and the transitional draw-down period (April 12th, 2011) – table corresponds to images in Figures 11 a-d.

Class	12 Apr 11	21 Oct 11	24 Dec 11	09 Jan 12
Open Water	4.719 ºK	8.841 ºK	7.581 ºK	5.040 ºK
Wetland Class 1 (flooded)	1.004 ºK	0.188 ºK	0.184 ºK	0.169 ºK
Wetland Class 2 (dry)	0.594 ºK	0.313 ºK	0.356 ºK	0.216 ºK
Upland	1.946 ºK	0.440 ºK	0.587 ºK	0.408 ºK

When flooded surface area was at its annual minimum during summer drawdown (Figures 10,13), open water surface temperature variance was lowest relative to the variance of each other class.

The surface temperature in December and February remained higher for upland areas relative to all other classes. However, the relationship between open water and wetland temperatures was reversed from summer (Figure 10) images. While wetland class 1 mean surface temperature was consistently lower than the corresponding wetland class 2 mean across all 15 Landsat images, on February 26th (Figure 12b) the mean surface temperature of wetland class 1 was marginally higher than the class 2 mean. In cold winter months the sensible heat flux from the surface into the atmosphere can warm the boundary layer and increase the surface temperature. As a result, flooded vegetation (wetland class 1) would be expected to have a higher mean surface temperature.

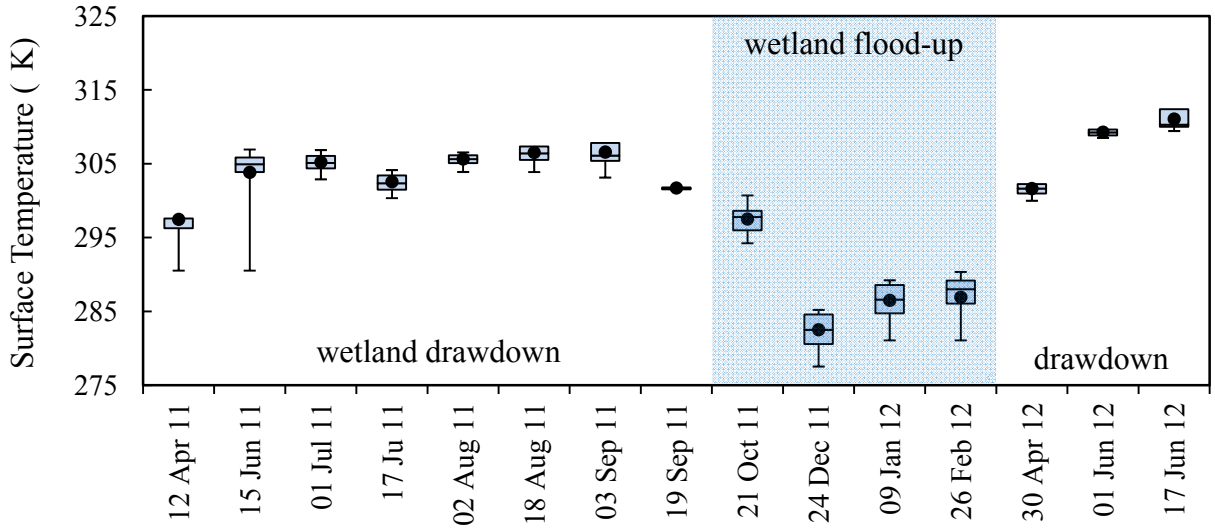

Figure 12: Surface temperature variance for "wetland footprint"

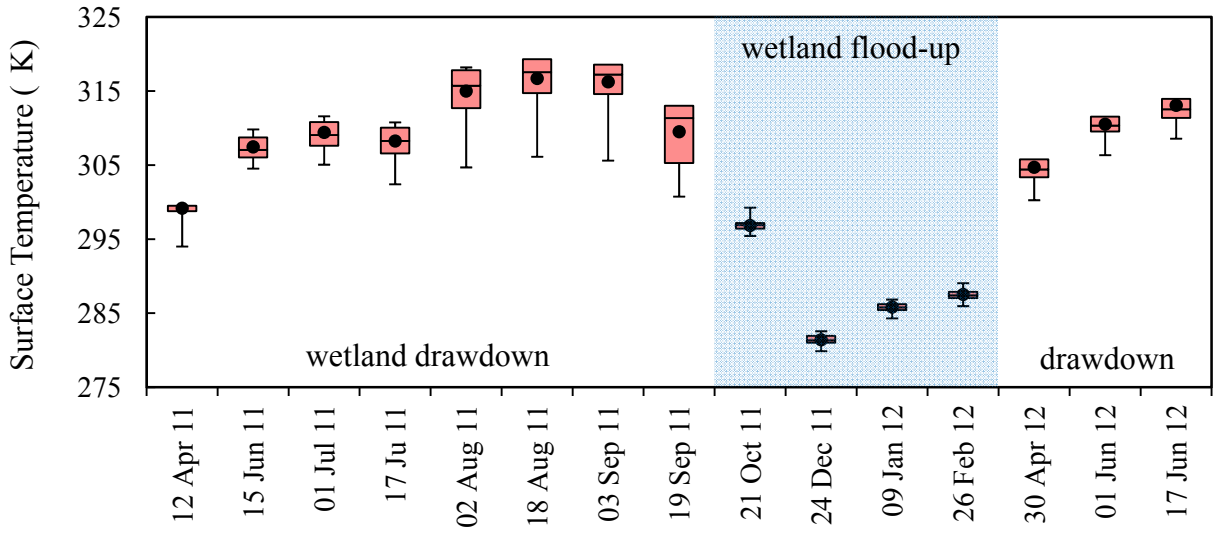

Figure 13: Surface temperature variance for "no wetland footprint"

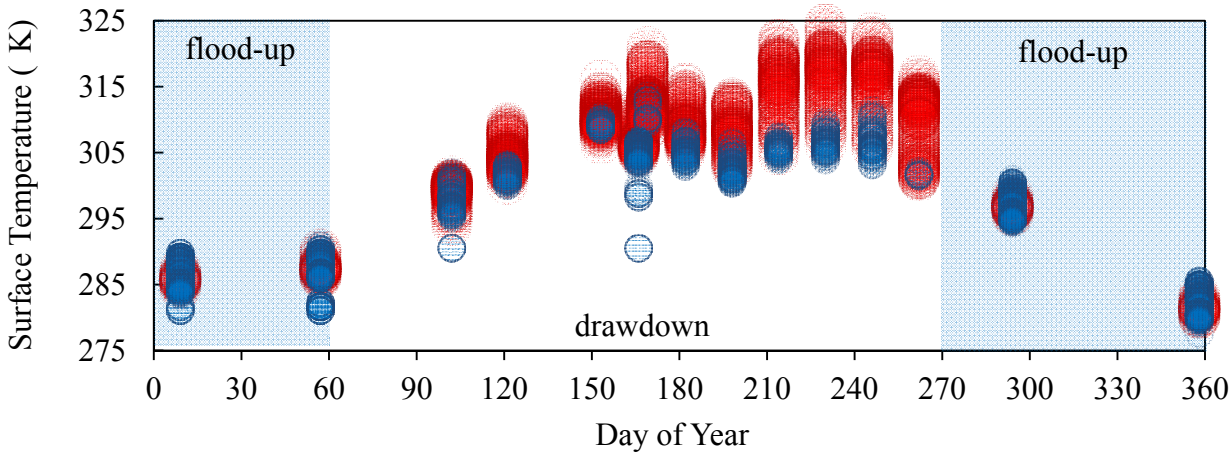

Figure 14: DSN footprint temperature (blue) vs. no footprint temperature (red). A total of N = 2,062 surface temperature values for pixels classified as wetland footprint (blue), and N = 3,920 non-wetland footprint (red) pixels have been plotted. Due to the large sample size and extent of overlap, both sets of data points are plotted with 99% transparency.

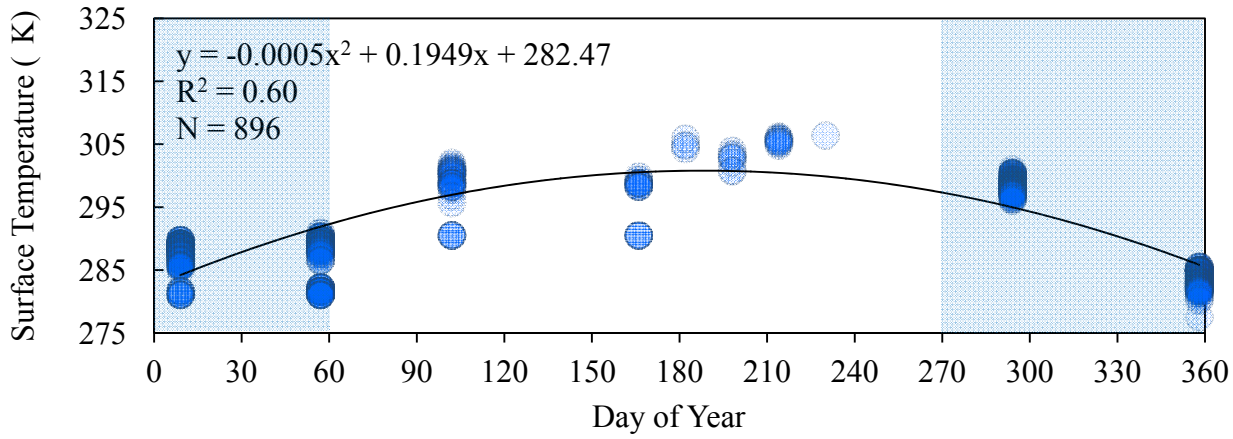

Figure 15: DSN Open water variance

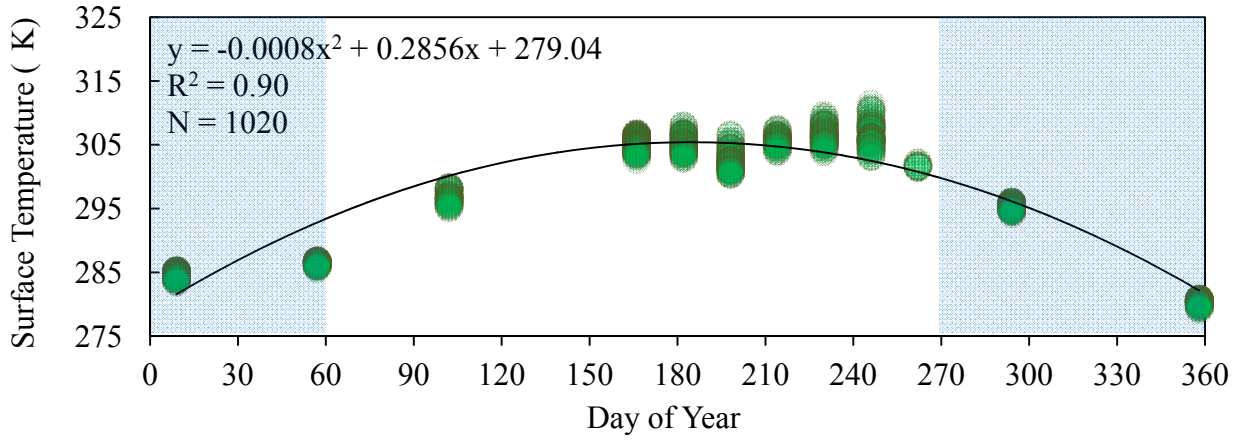

Figure 16: DSN flooded wetland variance,

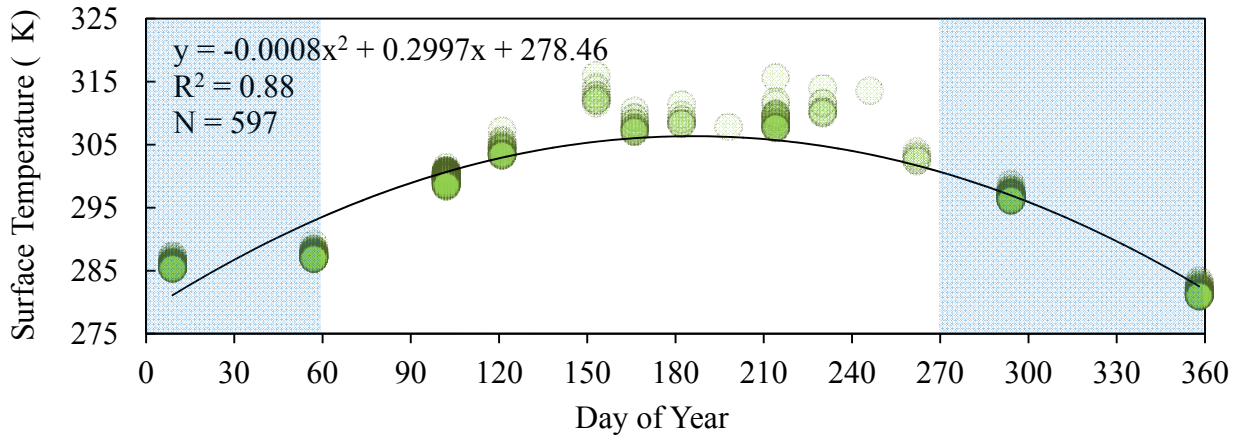

Figure 17: DSN dry wetland

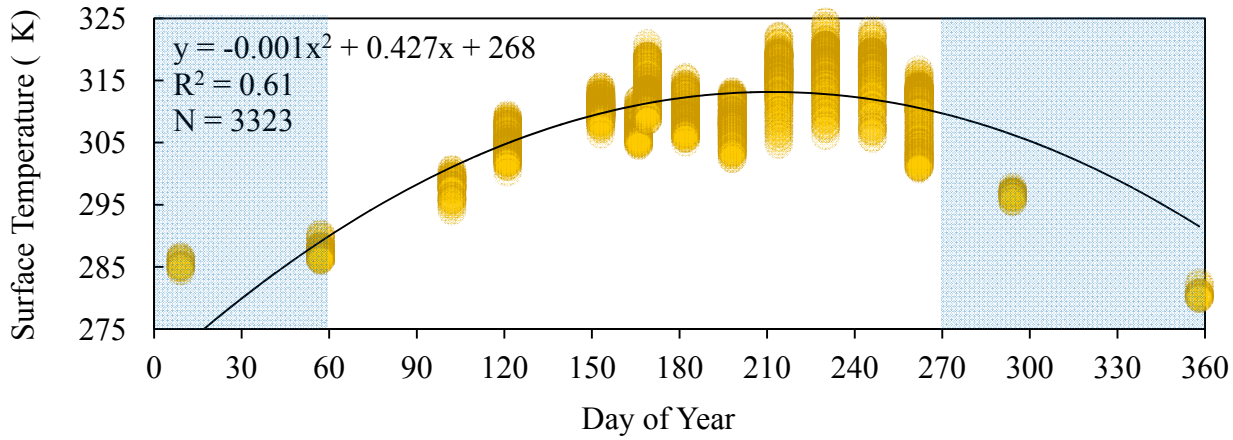

Figure 18: Upland variance

Table 4: statistics for open water at Ducky Strike North Field

	12 Apr 11	15Jun11	1Jul11	17Jul11	2Aug11	18Aug11	3Sep11	19Sep11	21Oct11	24Dec11	9Jan12	26Feb12	30Apr12	1Jun12	17Jun12
Count	49	23	4	9	12	1	0	0	202	200	196	200	0	0	0
Mean	298.35	296.26	304.94	302.53	305.57	306.39	-	-	298.33	283.58	287.61	287.06	-	-	-
SD	3.47	3.91	0.71	1.12	0.42	-	-	-	0.98	1.33	2.17	3.47	-	-	-
Min	290.52	290.52	304.22	300.72	304.79	306.39	-	-	296.06	277.53	281.07	281.07	-	-	-
Q1	298.27	290.52	304.63	302.08	305.32	306.39	-	-	297.65	282.51	286.96	282.23	-	-	-
Median	299.29	298.27	304.81	302.83	305.56	306.39	-	-	298.14	283.62	288.57	289.10	-	-	-
Q3	298.27	298.82	305.12	303.26	305.85	306.39	-	-	298.89	284.94	289.13	289.76	-	-	-
Max	302.04	299.90	305.91	303.98	306.24	306.39	-	-	300.98	285.55	289.76	290.93	-	-	-

Table 5: statistics for flooded wetland (wetland class 1) at Ducky Strike North Field

	12 Apr 11	15Jun11	1Jul11	17Jul11	2Aug11	18Aug11	3Sep11	19Sep11	21Oct11	24Dec11	9Jan12	26Feb12	30Apr12	1Jun12	17Jun12
Count	60	131	94	105	65	93	106	12	76	96	119	60	0	0	0
Mean	296.70	305.16	305.19	302.57	305.65	306.52	306.58	301.71	295.33	280.31	284.68	286.44	-	-	-
SD	0.88	0.96	1.22	1.47	0.84	1.30	1.87	0.25	0.47	0.38	0.41	0.31	-	-	-
Min	295.06	302.70	302.88	300.34	303.88	303.87	303.12	301.43	294.22	279.16	283.44	285.54	-	-	-
Q1	296.03	304.47	304.35	301.47	305.04	305.50	305.38	301.54	294.97	280.07	284.52	286.19	-	-	-
Median	296.61	305.16	305.09	302.31	305.66	306.41	306.10	301.63	295.34	280.37	284.73	286.53	-	-	-
Q3	296.03	305.94	306.06	303.44	306.31	307.35	307.81	301.80	295.70	280.60	285.00	286.72	-	-	-
Max	298.30	306.82	308.06	306.63	307.50	309.66	311.45	302.22	296.10	280.88	285.31	286.86	-	-	-

Table 6: statistics for dry wetland (wetland class 2) at Ducky Strike North Field

	12 Apr 11	15Jun11	1Jul11	17Jul11	2Aug11	18Aug11	3Sep11	19Sep11	21Oct11	24Dec11	9Jan12	26Feb12	30Apr12	1Jun12	17Jun12
Count	198	17	8	1	27	8	1	7	81	77	60	69	32	11	0
Mean	299.73	307.99	309.09	307.84	309.12	311.01	313.55	302.99	296.92	281.63	285.95	287.47	304.19	312.90	-
SD	0.63	0.95	1.06	0.00	1.73	1.37	-	0.53	0.54	0.59	0.49	0.48	0.89	1.30	-
Min	298.40	307.05	308.33	307.84	307.63	309.91	313.55	302.38	296.15	280.96	285.37	286.88	303.31	311.57	-
Q1	299.27	307.27	308.37	307.84	307.84	310.12	313.55	302.61	296.46	281.20	285.57	287.09	303.48	312.06	-
Median	299.75	307.61	308.73	307.84	308.57	310.37	313.55	302.90	296.95	281.46	285.83	287.35	303.98	312.38	-
Q3	299.27	308.48	309.22	307.84	309.71	311.57	313.55	303.25	297.22	281.98	286.22	287.73	304.61	313.35	-
Max	301.40	310.36	311.41	307.84	315.69	313.98	313.55	303.90	298.79	283.47	287.43	289.27	307.23	315.99	-

Table 7: statistics for upland at Ducky Strike North Field

	12 Apr 11	15Jun11	1Jul11	17Jul11	2Aug11	18Aug11	3Sep11	19Sep11	21Oct11	24Dec11	9Jan12	26Feb12	30Apr12	1Jun12	17Jun12
Count	89	228	292	284	295	297	292	380	40	23	24	70	287	344	378
Mean	297.98	307.43	309.43	308.26	315.54	316.86	316.25	309.64	296.70	280.71	285.56	287.60	304.76	310.45	313.08
SD	1.54	1.81	2.32	2.55	3.39	3.50	3.43	4.28	0.57	0.74	0.71	1.04	2.01	1.38	2.52
Min	294.01	304.53	305.06	302.41	304.69	306.12	305.61	300.75	295.44	279.88	284.31	285.96	300.26	306.35	308.57
Q1	297.25	305.98	307.58	306.57	313.81	314.95	314.61	305.82	296.32	280.15	285.06	286.88	303.27	309.48	311.37
Median	298.09	306.80	309.07	308.26	315.97	317.63	317.23	311.48	296.80	280.59	285.36	287.44	304.47	310.28	312.53
Q3	297.25	308.77	310.85	310.06	318.08	319.38	318.57	313.02	297.00	280.85	286.19	288.17	306.15	311.41	313.94
Max	300.73	312.01	315.56	313.23	322.24	324.49	323.23	316.75	297.92	282.56	286.77	290.37	309.54	314.11	321.02

This could be attributed in part to the effect of disparate sample size on variance and significance analysis of sample means.

Finally, the pattern of increasing surface temperature means and associated group variances in Figure 13 reinforced the limitations of assigning wetland classes to inundated or flooded categories year-round: despite the variations in the previous two figures (11-12) and their individual sub-plots, Figure 12 is the only one in which the surface temperature followed a consistently increasing pattern from open water to upland. The surface temperature mean of wetland class 1 – presumed to represent the flooded (evaporatively-cooled) wetland subclass, shared greater similarity with the temperature ranges of the two classes making up the non-flooded category (wetland class 2 and upland) that it did with the open water temperatures. In June, during draw-down, standing water may be effectively reduced to only open water portions. Draw-down would have caused recession of the wetland footprint, and formally inundated vegetated areas would no longer be flooded. This could be further validated by field-testing these hypotheses.

While four classes were ultimately classified, the flooded area delineation is effectively a 2-class categorization separating flooded area (encompassing both open water and inundated wetland vegetation sub-classes) from non-flooded (uplands and terrestrial wetland vegetation). Consequently, cases of ambiguity between wetland class 1 and open water, or between wetland class 2 and upland, where variance may have contributed to difference in sample means and not represented statistically robust independence would have affected neither the spatial distribution of flooded cells nor the total surface area.

4. Limitations

Wetland and upland classification was less effective in the presence of cropland – misclassifying irrigated or flooded fields as wetland areas and limiting the generalizability of this method for fully automated wetland classification. The Landsat ETM+ band 5 to band 2 ratio should be

combined with field-based ground truth data which can be used to constrain the potential wetland area and mask out extraneous pixels. LULC (Land Use Land Cover) maps, geo-referenced property boundaries, or manual delineation from aerial imagery may provide a sufficient spatial constraint.

5. Conclusions

In this study we developed a method to delineate the wetland footprint for seasonally-managed wetlands using Landsat ETM+ satellite imagery. The wetlands were delineated over the course of pond flood-up and drawdown cycles. We found that for preliminary image classification of open water, wetland and upland categories, a Landsat ETM+ band 5 to band 2 ratio was more efficient than similar classification using vegetation and water indices such as NDVI and NDWI. Unsupervised classification of surface temperature could be reduced to two classes, provided the input was clipped to wetland area only, and the classification was constrained to a single wetland pond at a time. Comparisons with field-derived surface area estimates show significant improvement over previous delineations which mapped open surface area only and did not account for flooded emergent vegetation. We expect that at large spatial scales and across greater topographic and ecologic variability the results of a two-class classification system may become biased by local effects. Improved performance is expected to come from refining the classification scheme by initializing unsupervised classification of surface temperature for a greater number of preliminary wetland classes and merging self-similar classes post-classification based on statistical analysis of the temperature means and variance. Since choice of imagery determines image resolution and subsequent precision, the described classification procedures using finer resolution imagery may narrow the error margin and improve flooded area estimates relative to those monitored at the two control ponds. In situations where adequate knowledge of the system exists to help validate the results, the approach presented in this study may be highly appropriate for seasonally-managed wetlands. The methods presented in this study are expected to be applicable in permanent wetlands as well. Despite potential minor seasonal fluctuation, permanent wetlands remain flooded throughout the year – similarly to seasonal wetlands during flood-up. While the methodology can be further refined to narrow the error gap between monitored flooded area and the results of surface temperature classification,

the relatively low computational cost, utility, and ready availability of required Landsat data result in a very pragmatic resource for improving wetland delineation.

References

Adam, E., Mutanga, O., and Rugege, D. (2010). Multispectral and hyperspectral remote sensing for identification and mapping of wetland vegetation: a review. Wetlands Ecological Management, 18:281-296.

Alesheikh, A.A., Ghorbanali, A., and Nouri, N. 2007. Coastline change detection using remote sensing. International Journal of Environmental Science and Technology, 4(1): 61-66.

Allen, R.G., Prueger, J.H., Hill, R.W., 1992. Evapotranspiration from isolated stands of hydrophytes: cattail and bulrush. Transactions of the American Society of Agricultural Engineers. 35(4): 1191-1198.

Allen, R.G., Hill, R.W., Srikanth, V., 1994. Evapotranspiration parameters for variably-sized wetlands. 1994 International Summer ASAE/ASCE Meeting, Kansas City, Missouri, Jun 19-22.

Allen, R.G., 1995. Evapotranspiration from wetlands. Evapotranspiration and Irrigation Efficiency, Arvada, Colorado, Oct 10-11.

Allen, R.G., 1998. Predicting evapotranspiration demands for wetlands. ASCE Wetlands Engineering and River Restoration Conference, Denver, Colarado, Mar 20-29.

Allen, R. G., Pereira, L., Raes, D., and Smith, M. (1998). Crop Evapotranspiration, Food and Agriculture Organization of the United Nations, Rome, Italy. ISBN 92-5-104219-5. 300 p.

Allen, R.G., 2005. Penman-Monteith equation. Encyclopedia of Soils, Elsevier, pp. 180-188.

Allen, R.G., Tasumi, M., 2005. Evaporation from American Falls Reservoir in Idaho via a combination of Bowen ratio and eddy covariance. Proceedings of the American Society of Civil Engineers. Impacts of Global Climate Change, 1-17.

Allen, R. G., Tasumi, M., and Trezza, R. (2007). “Satellite-based energy balance for mapping evapotranspiration with internalized calibration (METRIC) - Applications.” J. Irrig. Drain. Eng., 133(4): 395-406.

Allen, R.G., 2010. New procedure for estimating evaporation from open water and snow in METRIC. Estimation of Evaporation from Water in METRIC.

Allen, R.G., Tasumi, M., Trezza, R., Kjaersgaard, J., 2010. METRIC applications manual for Landsat satellite imagery. Version 2.0.7.

Bagan H., Wang, Q., Watanabe, M., Yang, Y., and Ma, J. (2005) Land cover classification from MODIS EVI times-series data using SOM neural network. International Journal of Remote Sensing, 26(22):4999-5012.

Baker, C., Lawrence, R., Montagne, C., and Patten, D. (2006). Mapping wetlands and riparian areas using Landsat ETM+ imagery and decision-tree-based models. Wetlands, 26(2):465-474.

Bastiaanssen, W.G.M. (1995). Regionalization of surface flux densities and moisture indicators in composite terrain: A remote sensing approach under clear skies in Mediterranean climates. Ph.D. dissertation, CIP Data Koninklijke Bibliotheek, Den Haag, The Netherlands. 273 p.

Bastiaanssen, W.G.M., Menenti M., Feddes R.A., Holtslag A.A.M., 1998. The Surface Energy Balance Algorithm for Land (SEBAL): Part 1 formulation. Journal of Hydrology. 212-213: 198-212.

Bastiaanssen, W.G.M., Pelgrum H., Wang J., Ma Y., Moreno J., Roerink G.J., van der Wal T. 1998. The Surface Energy Balance Algorithm for Land (SEBAL): Part 2 validation. Journal of Hydrology. 212-213: 213-229.

Berberoglu, S., Yilmaz, K.T., and Ozkan, C. (2004). Mapping and monitoring of coastal wetlands of Cukurova Delta in the Eastern Mediterranean region. Biodiversity and Conservation, 13:615-633.

Burman, R.D., Jensen, M., Allen, R.G., 1986. Thermodynamic factors in evapotranspiration. Transactions of the American Society of Civil Engineers. Irrigation Systems for the 21st Century. New York, NY: ASCE. 140-148.

California Department of Water Resources (DWR). 2008. Managing an Uncertain Future: Climate Change Adaptation Strategies for California's Water. [Online at: http://www.water.ca.gov/climatechange/docs/ClimateChangeWhitePaper.pdf]

Ĉerná, L., and Chytrý, M. (2005) Supervised classification of plant communities with artificial neural networks. Journal of Vegetation Science, 16(4):407-414.

Chander, G., Markham, B. L., and Helder, D. L. (2009). Summary of current radiometric calibration coefficients for Landsat MSS, TM, ETM+ and EO-1 ALI sensors. Remote sensing of Environment, 113, 893-903.

Cook, B.D., Bolstad, P.V., Naesset, E., Anderson, R.S., Garrigues, S., Morisette, J.T., Nickeson, J., and Davis, K.J. (2009). Using LiDAR and quickbird data to model plant production and quantify uncertainties associated with wetland detection and land cover generalizations. Remote Sensing Environment, 113:2366-2379.

Cushman, S.A., McGarigal, K., and Neel, M.C. (2008). Parsimony in landscape metrics: Strength, universality, and consistency. Ecological Indicators, 8:691-703.

Dobson, E. 2011. Mask Water. ERDAS Imagine User-Submitted Spatial Models for ERDAS Imagine. [Path: http://geospatial.intergraph.com/service/support/SpatialModels/Spatial_ Models.aspx.]

Donohue, R.J, Roderick, M.L., McVicar T.R., 2007. On the importance of including vegetation dynamics in Budyko's hydrological model. Hydrology and Earth Systems Sciences. 11:983-995.

Drexler, J.Z., Snyder, R.L., Spano, D., Paw U, K.T., (2004). A review of models and micrometeoroligcal methods used to estimate wetland evapotranspiration. Hydrological Processes. 18: 2071–2101.

Eklundh, L. (1998). Estimating relations between AVHRR NDVI and rainfall in East Africa at 10-day and monthly time scales. International Journal of Remote Sensing, 19(3):563-568.

Elhaddad, A., Garcia, L.A., 2007. A guide to using ReSET for estimating evapotranspiration. Integrated Decision Support Group (IDS).

Elhaddad, A., Garcia, L.A., 2008. Surface energy balance-based model for estimating evapotranspiration taking into account spatial variability in weather. Journal of Irrigation and Drainage Engineering. 134 (6):681-689.

Frohn, R.C., Reif, M., Lane, C., and Autrey, B. (2009). Satellite remote sensing of isolated wetlands using object-oriented classification of Landsat-7 data. Wetlands, 29(3):931-941.

Gao, B. (1996). NDWI – A normalized difference water index for remote sensing of vegetation liquid water from space. Remote Sensing of Environment, 58(3):257-266.

Harvey, K.R., and Hill, G.J.E. (2001). Vegetation mapping of a tropical freshwater swamp in the Northern Territory, Australia: a comparison of aerial photography, Landsat TM and SPOT satellite imagery. International Journal of Remote Sensing, 22:2911-2925.
Holben, B. (1986). Characteristics of maximum-value composite images from temporal AVHRR data. International Journal of Remote Sensing, 7:1417-1434.

Jensen, M.E., Burman, R.D., Allen, R.G., 1990. Evapotranspiration and Irrigation Water Requirements: Manual of Practice No. 70. New York, NY: ASCE.

Ji, L., and Peters, A.J. (2003). Assessing vegetation response to drought in the northern Great Plains using vegetation and drought indices. Remote Sensing of Environment, 18(1):85-98.

Ji, L., Zhang, L., and Wylie, B. (2009). Analysis of dynamic threshold for the normalized difference water index. Photogrammetric Engineering and Remote Sensing, 75(11):1307-1317.

Kelly, M., Tuxen, K.A., and Stralberg, D. (2011). Mapping changes to vegetation pattern in a restoring wetland: Finding pattern metrics that are consistent across spatial scale and time. Ecological Indicators, 11:263-273.

KISTERS North America, Inc. (2011). KISTERS - North America. KISTERS - Pioneering Technologies. [Online at: http://www.kisters.net/]

Klemas, V. (2005). Remote sensing: wetlands classification. In: Schwartz, M.L. (ed.), Encyclopedia of Coastal Science. Dordrecht, the Netherlands: Springer. pp. 804-807.

Klemas, V. (2011). Remote sensing of wetlands: case studies comparing practical techniques. Journal of Coastal Research, 27(3):418-427.

Klemas, V. (2013). Airborne remote sensing of coastal features and processes: an overview. Journal of Coastal Research, 29(2):239-255.

Kokaly, R.F., Despain, D.G., Clark, R.N., and Livo, K.E. (2003) Mapping vegetation in Yellowstone National Park using spectral feature analysis of AVIRIS data. Remote Sensing & Environment, 84:437–456.

Lunetta, R.S., and Balogh, M.E. (1999). Application of multi-temporal Landsat 5 TM imagery for wetland identification. Photogrammetric Engineering and Remote Sensing. 65:1303-1310.

Lin, Y., and Liquan, Z. (2006). Identification of the spectral characteristics of submerged plant Vallisneria spiralis. Acta Ecologica Sinica, 26:1005–1011.

Macleod, R.D., and Congalton, R.G. (1998). A quantitative comparison of change algorithms for monitoring eelgrass from remotely sensed data. Photogrammetric Engineering and Remote Sensing, 65:207-216.

Mänd, P., Hallik, L., Peñuelas, J., Nilson, T., Duce, P., Emmett, B.A., Beier, C., Estiarte, M., Garadnai, J., Kalapos, T., Schmidt, I.K., Kovács-Láng, E., Prieto, P., Tietema, A., Westerveld, J.W., and Kull, O. (2010). Responses of the reflectance indices PRI and NDVI to experimental warming and drought in European shrublands along a north-south climatic gradient. Remote Sensing of Environment, 114(3):626-636.

Maxa, M., and Bolstad, P. (2009). Mapping northern wetlands with high resolution satellite images and LIDAR. Wetlands, 29(1):248-260.

Ortiz, B.V., Thomson, S.J., Huang, Y., Reddy, K.N., and Ding, W. (2011). Determination of differences in crop injury from aerial application of glyphosate using vegetation indices. Computers and Electronics in Agriculture, 77(2):204-213.

Ozesmi, S.L., and Bauer, M.E. (2002). Satellite remote sensing of wetlands. Wetland Ecology & Management, 10:381-402.

Pettorelli, N., Vik, J.O., Mysterud, A., Gaillard, J.M., Tucker, C.J., and Stenseth, N.C. (2005). Using the satellite-derived NDVI to assess ecological responses to environmental change. Trends in Ecology and Evolution, 20(9):503-510.

Phillips, R.L., Beeri, O., and DeKeyser, E.S. (2005). Remote wetland assessment for Missouri Coteau prairie glacial basins. Wetlands, 25:355-349.

Phinn, S.R., Stow, D.A., and Mouwerik, D.V. (1999). Remotely sensed estimates of vegetation structural characteristics in restored wetlands, Southern California. Photogrammetric Engineering and Remote Sensing, 65:485-493.

Phinn, S.R., Menges, C., Hill, G.J.E., Standford, M., 2000. Optimizing remotely sensed solution for monitoring, modeling and managing coastal environments. Remote Sensing of Environment. 73: 117-132.

Piao, S., Mohammat, A.,Fang, J., Cai, Q., and Feng, J. (2006). NDVI-based increase in growth of temperate grasslands and its response to climate changes in China. Global Environmental Change, 16(4):340-348.

Porporato, A., Laio, F., Ridolfi, L., Rodriguez-Iturbe, I., 2001. Plants in water-controlled ecosystems: active role in hydrologic processes and response to water stress: III. Vegetation water stress. Advances in Water Resources. 24:725-744.

Quinn, N.W.T., and Karkoski, J. (1998). Potential for real time management of water quality in the San Joaquin Basin, California. Journal of the American Water Resources Association. 36(6).

Quinn, N.W.T. (2009). Environmental decision support system development for seasonal wetland salt management in a river basin subjected to water quality regulation. Agricultural Water Management. 96(2): 247-254.

Quinn, N.W.T., Ortega, R., and Holm, L. (2010a). Environmental sensor networks and continuous data quality assurance to manage salinity within a highly regulated river basin. Decision Support Systems in Agriculture, Food and the Environment: Trends, Applications and Advances. 420-434.

Quinn, N.W.T., Widell, D.L., Ortega,R., Rahilly, P., Beam, J.A.., Cook, W., Sparks, L., and O'Dell, M. (2010b). Final report for adaptive, coordinated real-time management of wetland drainage. Prepared for the State Water Resources Control Board by Berkeley National Laboratory for the Grassland Water District.

Quinn, N.W.T., Lee, G., and Cozad, D. (2010c). Information technology and decision support tools for stakeholder-driven river basin salinity management. IEEE Proceedings, 43rd Annual HICSS Conference, Kawaii, Hawaii, Feb 5-9.

Rahilly, P., Quinn, N.W.T., Beam, J.A., Widell, D.L., Ortega, R., Cook, W., Sparks, L., O'Dell, M., 2010. Wetland response to modified hydrology with respect to salinity management: Biological monitoring. Grassland Water District, Cal Fed Agreement P0640003-01.

Richard, Y., and Poccard, I. (1998). A statistical study of NDVI sensitivity to seasonal and interannual rainfall variations in Southern Africa. International Journal of Remote Sensing, 19(15):2907-2920.

Roerink, G.J., Menenti, M., Soepboer, W., and Su, Z. (2003). Assessment of climate impact on vegetation dynamics by using remote sensing. Assessment of climate impact on vegetation dynamics by using remote sensing, Physics and Chemistry of the Earth, Parts A/B/C, 28(1–3): 103-109.

Schmidt, K.S., Skidmore, A.K., Kloosterman, E.H., Van Oosten, H., Kumar, L., and Janssen, J.A.M. (2004). Mapping coastal vegetation using an expert system and hyperspectral imagery. Photogrammetric Engineering and Remote Sensing, 70:703-716.

Tasumi, M., Bastiaanssen, W., Allen, R. G., 2004. A step-by-step guide to running SEBAL, University of Idaho and International Institute for Aerospace Survey and Earth Sciences, Enschede, the Netherlands.

Thelen, K.D., Kravchenko, A.N., and Lee, C. (2004). Use of optical remote sensing for detecting herbicide injury in soybean. Wood Technology, 18:292-297.

U.S. Environmental Protection Agency (USEPA). (2002). National water quality inventory: 2000 report. U.S. Environmental Protection Agency, Office of Water, Washington, DC, USA. EPA 841-R-02-001.

Wang, X., Xie, H., Guan, H., and Zhou, X. (2007). Different responses of MODIS-derived NDVI to root-zone soil moisture in semi-arid and humid regions. Journal of Hydrology, 340(1-2):12-24.

Wright, C., and Gallant, A. (2007). Improved wetland remote sensing in Yellowstone National Park using classification trees to combine TM imagery and ancillary environmental data. Remote Sensing Environment, 107(4):582-605.

Xiao, X., Braswell, B., Zhang, Q., Boles, S., Frolking, S., and Moore, B. (2003). Sensitivity of vegetation indices to atmospheric aerosols: continental-scale observations in Northern Asia. Remote Sensing of Environment, 84(3):385-392.

Xie, Y., Sha, Z., and Yu, M. (2008). Remote sensing imagery in vegetation mapping: a review. Journal of Plant Ecology, 1(1):9-23.

Xu, H. (2006). Modification of normalized difference water index (NDWI) to enhance open water features in remotely sensed imagery. International Journal of Remote Sensing, 27(14):3025-3033.

YSI Inc. / Xylem Inc. (2012). YSI EcoNet - Web Enabled Monitoring and Control. Environmental Monitoring Data to the Web. [Online at: http://www.ysieconet.com/]